E-1516

HOT WIRE CALORIMETER STUDY OF ION
PRODUCTION AND ACCELERATION

By V. A. Sandborn and L. V. Baldwin

Lewis Research Center
National Aeronautics and Space Administration
Cleveland, Ohio

SUMMARY

A porous tungsten ion source and a Pierce accelerator system similar
in principle to proposed space propulsion systems is studied in detail.
Cesium ion production from a porous tungsten ionizer is shown to be
accurately predicted from cold flow calibrations. A hysteresis is ob-
served in the measured critical ion emitter temperature and is explained
in terms of Taylor and Langmuir's data on the evaporation of cesium from
non-porus tungsten.

The characteristics of the Pierce acceleration system minus the
ground "decelerator" are fully evaluated with the hot-wire calorimeter.
It is demonstrated that the use of grid wires to eliminate the voltage
gradient across the aperture of the Pierce accelerator leads to better
agreement of total ion beam power with the predictions of Child's law.
With an open aperture, the observed ion beam spreading was accounted for
by the combined effects of beam space charge and accelerator defocusing
action. With grid wires across the aperture the beam spread is due to
space charge alone. These results should be restricted to "thin" beam
ion rockets.

A local electron emission configuration placed within the accelerator
electrode was found to greatly increase the total beam power available
from a fixed geometry Pierce accelerator system. These observations,

while of a tentative nature, offer a means of obtaining large improvements in accelerator efficiency.

INTRODUCTION

The use of electrostatically accelerated ions as a propulsion system for space flight appears promising (refs. 1 and 2). Sizable research and development programs are now in progress to develop practical systems of ion propulsion. This research has created a demand for instrumentation and experimental techniques to evaluate the ion rocket. The ion beam diagnostic techniques are being rapidly developed to meet the demand.

One promising instrument for ion beam diagnostic work is the hot wire calorimeter (developed by the present authors refs. 3 and 4). This resistance-temperature transducer measures the beam power at a point and the power distribution through-out the beam. The ion source and accelerator system employed herein is not viewed as a practical space propulsion system. Rather, the system is considered as a research tool both to develop diagnostic techniques and to study the basic physics of ion beams. The present paper is a detailed study of some of the physical processes of a porous tungsten-cesium ion system employing a cylindrical Pierce accelerator. The hot wire calorimeter is used to evaluate the ion source and ion accelerator systems. The detailed analysis of this ion source led not only to the confirmation of design criteria, but also to the discovery of some unexpected and potentially important phenomena.

SYMBOLS

A_e area of the emitter

a ion beam radius

D ion emitter diameter

F_2 $\Big\}$ functions of the reduced radius (r/a) used in the design
F_4 $\Big\}$ of the Pierce accelerator

f   focal length of lens

G   design constant given in equation (5)

J   ion beam current

j   ion beam current density

l physical dimension from the ion emitter to the Pierce accelerator

P   pressure

ΔP pressure difference across the porous tungsten ion emitter

r   radial distance in cylindrical coordinates

r_e radius of the ion emitter

r_o radius of the ion beam at the point where the ion flow is

         originally parallel

T   temperature

T_e ion emitter temperature

T_{VAP} vaporizer temperature

V   voltage

ΔV accelerating voltage, difference between emitter and accelerate

         voltage

Z   axial distance in cylindrical coordinates

Z_o constant, equation (5)

0   angle in cylindrical coordinates

APPARATUS, PROCEDURE, AND INSTRUMENTATION

Vacuum facility. - The present experiments were conducted in a side port of one of the high-vacuum electric-rocket research facilities of the NASA Lewis Research Center. Figure 1(a) shows a cutaway sketch of the engine housing and valve arrangement leading into the 5 foot diameter tank.

The pressure within the tank is maintained between 10^{-7} and 10^{-6} millimeter-of-mercury for all tests. The pressure in the engine housing area normally was an order of magnitude greater; high 10^{-6} to low 10^{-5} millimeter-of-mercury pressure range.

A viewing port was available on the opposite side of the 5 foot tank. Through this port the porous tungsten emitter could be viewed with an optical pyrometer to determine the temperature. The cleanness of the window could not be controlled, thus, emitter temperature measurements may be as much as 100° F too low. Only for the data reported on critical emitter temperature was the window directly calibrated.

Ion source. - Figure 1(b) is composite photograph of the ion source and accelerator. A porous tungsten emitter was employed. This emitter was chosen to give a uniform distribution of ions for the accelerator study. The porous tungsten disk (0.048" thick) was brazed into a molybdenum tube of 1 inch inside diameter. It was found from a wetting technique that the braze filled the edges of the porous tungsten, such that the effective radius for ion emission was 0.82 inches. The molybdenum tube was mounted directly to the copper vaporizer, with a stainless steel "O" ring seal. The vaporizer and emitter are shown in figure 1(b). This arrangement of porous tungsten emitter proved practical; no failure of the porous piece has ever occurred. A slight flaking of the molybdenum was noted due to the high temperature operation, but it in no way affected operation. A wire radiation emitter heater, (identified on fig. 1(a), as emitter heater but removed in fig. 1(b)) is inserted around the molybdenum tube. The emitter assembly is heated until the porous tungsten emitter reaches the desired temperature.

The heat transfer from the molybdenum tube to the vaporizer is sufficient to heat the vaporizer. Air cooling tubes are provided around the vaporizer to control the temperature. The temperature of the vaporizer determines the amount of the cesium vapor that flows through the emitter. For the present tests a glass capsule of cesium metal was placed in the vaporizer. Normal operation required the emitter to be brought to temperature (around 2000° F), and the vaporizer temperature to be held below 300° F with cooling air. When these conditions are reached a glass containing cesium is broken with a plunger. Some of the cesium is vaporized, and flows through the porous tungsten plug. Cesium molecules are ionized by the hot tungsten surface and in turn are accelerated from the emitter surface by the electrostatic accelerator system.

Acceleration system. - The positive cesium ions are accelerated away from the tungsten emitter by maintaining the emitter at a positive potential with respect to the accelerator. For the present tests, voltages between 1 and 10 kilovolts were employed. The complete emitter, molybdenum tube, emitter heater, and vaporizer are all the same high potential in the present set-up. To control the initial focusing of the ion beam, a beam forming or focusing electrode, noted in figure 1(b), is mounted in physical contact with the tungsten emitter. This focusing electrode has a cone shape similar to the single accelerator and serves to form and maintain the accelerated ions in trajectories nearly perpendicular to the emitter. The aperture of the focusing electrode is 0.82 inch in diameter to match the effective emitter diameter.

The accelerator is mounted parallel to the focusing electrode. This accelerator is electrically insulated from the emitter-focusing electrode system. For the experimental studies reported herein, the accelerator is

operated at negative potentials (from -1 to -10 kilovolts). Both the focusing and accelerating electrodes were spun formed from nickel sheet using dies. The accelerator aperture is 1 inch in diameter. A slight oversized aperture was used in an attempt to ease ion beam impingement. Accelerator aperture effect (to be discussed later) was evaluated by using accelerators with grid wires mounted across the aperture. A straight grid wire accelerator was employed to evaluate the critical temperature characteristics of the porous tungsten ionizer at high current densities.

For the design of the Pierce accelerator it was assumed that uniform current density flowed normally and one dimensionally from the emitter. It was further assumed that normal operation for the beam would be space-charge limited flow. This saturation current density is described by Child's solution of Poisson's equation (the constant corresponds to singly charged cesium ions):

$$j = 4.75 \times 10^{-9} \frac{\Delta V^{3/2}}{Z^2} \tag{1}$$

where ΔV is the voltage difference between emitter and accelerator, and Z is the distance between the emitter and the accelerator. The electrode design to obtain these conditions in a cylindrical beam was calculated using Daykin's series solution of Laplace's equation with the Pierce boundary conditions, reference 5. The beam forming electrode, which rests on the ion emitting surface makes an angle of 67.5 degrees with the emitter surface as prescribed by Pierce, reference 6, (p. 181). The single accelerating electrode coordinates were calculated from Daykin's formula

retaining three terms as follows

$$\Delta V = \left(\frac{10^9}{4.75}\right)^{2/3} j^{2/3} \, Z^{4/3} \left[1 + \left(\frac{a}{Z}\right)^2 F_2 + \left(\frac{a}{Z}\right)^4 F_4\right] \tag{2}$$

The terms F_2 and F_4 are functions of the reduced radius (r/a); these functions were taken from reference 5. A discussion of this design method also may be found in reference 7. Equation (2) was rearranged for ease of calculation to the following form

$$\left(\frac{a}{Z}\right)^4 F_4 + \left(\frac{a}{Z}\right)^2 F_2 + \left[1 - \left(\frac{Z_0}{Z}\right)^{4/3}\right] = 0 \tag{3}$$

where

$$Z_0 = \left(4.75 \times 10^{-9} \frac{\Delta V^{3/2}}{j}\right)^{1/2} \tag{4}$$

This form of the equation was then solved, using an iteration technique, for the electrode coordinate Z as a function of r for the following design point.

$$\left. \begin{array}{l} G \equiv \dfrac{jA_e}{\Delta V^{3/2}} = 5.20 \times 10^{-9} \; \dfrac{\text{amp}}{\text{volts}^{3/2}} \\[2ex] \text{where} \\[1ex] Z_0 = 1.76 \text{ cm or } 0.693 \text{ in. and } A_e = 3.42 \times 10^{-4} \text{ m}^2 \text{ or } 0.528 \text{ in.}^2 \end{array} \right\} \tag{5}$$

Instrumentation. - Operation of the ion rocket was monitored by electrical current and voltage meters. The electrical schematic of the system is shown in figure 1(b). Vaporizer temperature was measured with thermocouples, which were electrically floating at the voltage level of the emitter. The emitter temperature was measured with a disappearing filament type of optical pyrometer. A small temperature gradient $(20^\circ$ to 50° F) exists across the face of the emitter when it is operated above 2000° F, since the heat flow is by conduction from the molybdenum tube to the porous tungsten plug. However, only an average emitter temperature was recorded.

A single wire, hot-wire calorimeter probe shown in figure 2 was used to measure the power distribution through the ion beam. This probe is similar in construction to the hot-wire probe rakes described in detail in reference 3. The probe traverses the ion beam in a plane parallel to the emitter and at a station 7.1 inches downstream of the emitter. The probe passes across the centerline of the beam, and thus corresponds to a measurement across the diameter of the beam. The probe is mounted through a grease sealed vacuum fitting to a remote controlled 12 inch actuator. When not surveying, the probe was retracted into a 3 inch deep well in the side of the housing. The output of the transducer was recorded on an x-y recorder setup identical to that described in reference 3. The hot-wire detection circuit is also that of reference 3. A 0.0004 inch diameter platinum-iridium wire 0.20 inches long was employed for all the measurements.

TEST RESULTS AND DISCUSSION

Ion Beam Measurements

The present results for the most part are taken from hot-wire calorimeter measurements. Therefore, evidence is presented to establish the usability of a single probe to evaluate overall performance. For one probe traverse to be sufficient to obtain overall power it is necessary that the beam be nearly cylindrical and symmetric. A 2 inch copper sheet calorimeter was placed in the beam at the approximate downstream location where the hot-wire traces were taken. After a short operating time it was discovered that the ion beam had sputtered the calorimeter plate in the pattern shown in figure 3. Similar sputtering patterns established that the beam is approximately cylindrical for all operating conditions. The sputtering of the plate calorimeter, while

ideal for showing beam shape, quickly becomes a problem. Much of the sputtered copper is plated out on the ion emitter and accelerator system leading to excessive electrical breakdown within the engine. The plate calorimeters proved undesirable in the present test setup, since they could not be moved far enough downstream to prevent much of the sputtering material from reaching the engines.

No evidence of any asymmetry was observed in the sputtering pattern. Since the ion emitter and accelerator are symmetric, there appears to be no reason to believe the ion beam produced should not be approximately symmetrical. Typical hot wire surveys are shown in figure 4. There is an upward shifting in the base line of each profile due to both the thermal radiation effect of the hot tungsten emitter and a slight increase in the support temperature of the probe as the beam is traversed. The shift in the zero power level due to the two effects is shown as the dashed curves on each trace (the shift can be calculated, see ref. 4 for a given input). The power due to the ion beam is proportional to the vertical distance between the solid and dashed curves. For the most part the profiles are reasonably symmetrical about the centerline.

Total power was computed from each profile using digital computing equipment. A telereader was used to read the local power from the curve at specific distances from the centerline. The integral

$$2 \int_0^\pi (\text{local power density for an element } \Delta r) \times (\text{distance from } c_L) d\theta \qquad (6)$$

is formed and evaluated digitally. Separate integrals are evaluated for the left and right sides of the traces, so that any asymmetry observed in the two halfs of the profile is roughly compensated. For most of the data presented two traces were taken; one for the initial traverse and one

when the probe is withdrawn. For the majority of the measurements agreement between repeat profiles was ± 0.1 watts or about 1 percent for the average operating condition. The absolute accuracy of any hot-wire calorimeter survey cannot be assessed as yet, because of the uncertainty in the accommodation coefficient (no greater than 10 percent error is expected) reference 3.

Figure 5 compares a typical set of total power measurements obtained from the hot-wire profile with power obtained from meters. The net current to ground times the voltage on the emitter should equal the total power in the beam if no external electrons from the test facility migrate to the ion beam source. To compute the power from the meters it is assumed that no extraneous electrons from outside the monitored system enter the electrical circuits shown in figure 1(b). The regions of disagreement on figure 5 are systematic in such a manner as to imply extraneous electrons have entered the electric circuits. In figure 6 some of the data of figure 5 have been replotted in a different form. Figure 6(a) shows that the metered and calorimeter measurements systematically approach one another as the accelerator voltage is increased. Due to aperture effects, the total power of the rocket would not be expected to reach the Child's law curve. This suggests that the meter readings of figure 6(a) are high, particularly at low accelerator potentials, due to extraneous electrons, which are "cut-off" at the larger accelerator potentials. Figure 6(b) shows the effect of vaporizer temperature on the agreement. The vaporizer temperature is an effective measure of the beam density below space-charge limited operation. The denser the beam of positive ions the more likely it is that extraneous electrons will fall

to the emitter. In both examples of figure 6 it appears the difference between metered and hot-wire power is traceable to extraneous electrons, which cause some of the metered data to be erroneously high.

Under the most favorable conditions it appears the meters and hot-wire measurements agree. When disagreement occurs it appears that the deviation is systematic in the metered current data. Therefore, it is assumed herein that the hot-wire calorimeter measurements are more likely to be a true indication of beam power for all operating conditions. Only the critical ionizer emitter current density data and accelerator impingement data were taken from metered currents (figs. 8, 12, and 19).

Ionizer Study

Ion source calibration. - At the outset of the experimental program an effort was made to determine the porous tungsten characteristics. By evaluating the volume flow characteristics of the emitter in nitrogen, the maximum ion current possible from the surface can be predicted for any given vaporizer pressure (ref. 8). The flow characteristics also give an indication of the average pore size of the porous emitter. Figure 7 shows the cold flow calibration obtained for the present emitters. These data were obtained by T. W. Reynolds in a small nitrogen flow calibration procedure and rig are described in reference 8. From the measured mass flow and pressure drop data, an average pore diameter of 5 microns was calculated for the porous tungsten (for calculation procedure see ref. 8). In operation the vapor pressure of cesium (5×10^{-4} to 1 mm Hg) will normally be less than 1 mm Hg, which is the lower limit of the calibration rig. However, the flow for $\Delta P < 10$ mm Hg is free molecular for the porous tungsten samples; therefore, the slope of the flow against pressure drop curve should be equal to 1 as can be seen in figure 7. The data of figure 7

were used to determine that the value of nitrogen flow at 1 mm Hg pressure drop is 5.5×10^{-7} standard cubic feet/second. This value was then used to accurately specify the calibration curve in the free molecular flow region below 1 mm Hg.

From the flow calibration curve a maximum ion current for a given vaporizer temperature can be predicted for the emitter. The current is equal to the number of particles per second flowing through the emitter times the electrical charge of each particle; converting to cesium rather than nitrogen gives

$$\text{Emitter current} = \left(\frac{\text{Volume/sec.}}{\text{mm Hg}}\right)\left(\frac{\text{Particles}}{\text{Volume}}\right) \times 1.6 \times 10^{-19} \left(\frac{\text{Coulcombs}}{\text{Particles}}\right)$$

$$\times \Delta P \text{ (mm Hg)} \times \frac{\text{A.R. cesium}}{\text{A.R. nitrogen}} \qquad (7)$$

where A. R. cesium is the arrival rate of cesium defined from kinetic theory as

$$\text{Arrival rate} = \frac{3.52 \times 10^{22} \text{ P (mm Hg.)}}{\sqrt{T \times \text{molecular weight}}} \qquad (8)$$

Equation (7) reduces to

$$\text{Emitter current} = 31.1 \times 10^{-3} \sqrt{\frac{492}{T_{vap}}} \times \Delta P \text{ (amperes)} \qquad (9)$$

Employing a vapor pressure against temperature curve for cesium (ref. 16) the emitter current against vaporizer temperature curve of figure 8 is obtained.

The straight grid wire accelerator was used to check the predicted ion current. The spacing between the emitter and grid wires was 0.08 inches. Limited running time was available with the particular setup,

since the high current density beams quickly sputter the grid wires. For
high vaporizer temperatures the predictions of equation (9) are quite good.
The discrepancy at low vaporizer temperature may in part be tied to a
problem encountered early in the experimental program. It was discovered
that no matter how carefully the emitter was cleaned chemically between
runs a small ion beam is produced on heating of the emitter and the applica-
tion of positive potential to the emitter. It was possible to operate
the "ion beam" for a matter of hours before the "dirt ions" were ex-
hausted; although currents before the capsule of cesium is broken
normally do not exceed one milliampere. Thus, the discrepancy between
theory and observation at low current densities are apparently tracable
to the "dirt ions" which determine the noise level of the experiment.
Because of the grid wire sputtering problem and also the limited test
time available for the present research program, it was impossible to
allow extensive time for the emitter to clean itself before the tests
were made.

Surface ionization is an adsorption reaction process. Therefore,
the properties at the surface of the ionizer are of importance. Different
tungsten samples do not appear to effect the ionization efficiency
greatly. The temperature of the ionizer, however, will have an ap-
preciable effect on the ionization efficiency. Figure 9 shows the ef-
fect of emitter temperature on hot-wire calorimeter measured total power
of a given source configuration that is well within the "vaporizer
limited" range of operation. In the example shown the arrival rate of
cesium was maintained at a constant value and only the emitter temperature
is varied. At some "critical temperature" the production of ions diminishes

greatly. Upon increasing the temperature of the ion emitter, it was found that a hysteresis in emitter critical temperature occurred. This hysteresis can be explained from the experimental data on the evaporation of cesium from tungsten reported by Taylor and Langmuir, reference 9. Although the evaporation data was for solid tungsten, the qualitative results are valid for the present observation. Reynolds and Childs, reference 10, have replotted the evaporation data in terms of total evaporation rates (ions plus atoms) as a function of monolayer absorbed on the tungsten. Following the work of Reynolds and Childs a curve of fraction of monolayer absorbed on surface against tungsten emitter temperature at a constant arrival rate may be constructed as shown in figure 10. Now consider what happens as the emitter temperature is decreased from point A to point E. Between points A and D the ion production will be nearly constant. As the temperature is decreased from point D to E, the only point on the curve corresponds to atoms mainly and not ions, thus, the ion beam is reduced to a very low value. If now the emitter temperature is increased from E to F, the layer absorbed decreases along the atom curve. As the temperature increases from points F to G to H, the ion beam begins to reappear as some ions as well as atoms are evaporated from the tungsten surface. Upon reaching an emitter temperature at point I, the fraction of a monolayer absorbed decreases sharply to the ion curve, and the production of ion is greatly increased.

Figure 11 shows the measurements obtained for the critical emitter temperature against flow rate (vaporizer temperature) for the present emitter. The open points shown on figure 11 were obtained with the

straight grid wire accelerator whereas the solid points were taken with the Pierce accelerators. In all cases with the straight grid wires no true beam shutoff was observed. Rather, a point was reached where the negative accelerator appeared to short out directly to the positive emitter. In each case the apparent short disappeared when the operating conditions (e.g. T_e or T_{vap}) were changed from the near critical conditions, suggesting that the electrical coupling was brought about by neutral cesium vapor. The two points where the negative accelerator physically failed due to sputtering are included to help establish the upper limit of the faired curve shown on figure 11. The lower curve corresponds to the maximum point of the curves of sketch 1, and was obtained in the present case by cooling the emitter. All of the open points were taken for conditions corresponding to the lower curve. The upper curve corresponds to the minimum point of the curves of figure 10, and was obtained by increasing the emitter temperature.

The maximum current density corresponding to the emitter critical temperature has been evaluated by Reynolds (ref. 8), from the data of Taylor and Langmuir (ref. 9). The maximum current may also be corrected for the effect of pore size of porous tungsten. Reynolds' predictions for a 5μ pore diameter emitter are shown in figure 12. Data obtained with the grid wire accelerator assembly near the critical emitter temperature (point D on figure 10) are also included on figure 12. Although the data shown on figure 12 are insufficient for definite conclusions to be drawn, the experimental data seem to be in good agreement with the predicted values.

The one piece of data missing from the present ionizer study is the cesium ionization efficiency. The conditions of the ion source were varied so greatly over a running period, that it proved impractical to compute time integrated total power for comparison with total cesium consumption for a given run.

Pierce Accelerator Characteristics

Design problems of ion acceleration and optics for real systems can be solved by analog or approximate analytical techniques. The present approach was to chose a relatively simple geometry for which a variety of analytical formulas are known from electron gun design.

Total beam power. - It has long been recognized in electron gun design that the actual beam current will fall below the design value for specific conditions (ref. 5). Specifically, difficulty is encountered if the ratio of accelerator spacing to beam diameter is less than about two (e. g., ref. 6, p. 183). Since the present design called for an aspect ratio near one, some decrease in voltage gradient at the center of the emitter would be expected. This so-called "aperture effect" is expected to decrease the ion current density near the axis of the cylindrical beam, and this "hollowing" of the beam lowers the net power output. The effects of the accelerator aperture are expected to be more pronounced as the aspect ratio decreases from 1.5 to 0.6. No reliable analytical techniques are available to make quantitative estimates. But, analog experience in electrolytic tanks has lead to some "rules-of-thumb," (ref. 11). Therefore, one of the experimental objectives of this work was to determine the discrepancy between Child's law predictions and actual measurements.

Figure 13 shows an example of the total space charge-limited beam current obtained from hot-wire measurements

$$\left(\text{Beam current} = \frac{\text{Total beam power}}{\text{Voltage on the emitter}} \right).$$

For figure 13 the acceleration voltage is the voltage difference between emitter and accelerator. For each value of l/D similar data were obtained. In no case did the measured current for the open aperture case reach the theoretical current. By fitting a 3/2 power curve through the measurements an estimate of the effect of aperture without grid wires for different values of l/D was made. Figure 14 is a summary of the measured aperture effect on beam current. As suggested above, at the larger l/D ratios the aperture effect is diminished and the data approach Child's law predictions.

The use of grid wires across the Pierce accelerator aperture should produce a flatter potential gradient and, thereby, reduce the aperture effect. Figure 13 also shows the power measured for the Pierce accelerator with grid wires. The grid wires bring the power into close agreement with Child's law.

Beam spreading. - The width of the ion beam at the hot-wire calorimeter surveying station ($X = 7.1$ in. downstream of emitter) is obtained from the recorded traces. The width is estimated by extending the edges of the profiles, such as shown in figure 4(a), straight down across the dashed curves. The slight rounding at the end of each profile is neglected, as it represents lag in the recording equipment. Figure 15(a) shows the variation in beam width observed at different flow rates at an accelerator aspect ratio of 0.87. When the beam is space charge limited the width of

the beam remains constant independent of neutral cesium arrival rate.
Figure 15(b) shows the beam spread obtained when grid wires were placed
across the aperture of the accelerator. For all cases it was found that
the grid wires reduce the beam width over that of the open aperture.

Figure 16(a) and (b) summarizes the space-charge-limited beam width
for the different aspect ratios. The smaller the aspect ratio the greater
the beam spreads. The data are correlated in terms of the net acceler-
ating voltage divided by the emitter voltage. The reason for plotting
against $\Delta V/V$ will become clearer when theoretical beam spreading re-
lations are considered.

Aperture effect on beam spreading. - Fairly elaborate design pro-
cedures have been developed to predict electron beam spreading (e.g.
ref. 13). These procedures can be applied at least in part to the
present ion beams. It is important to emphasize the approximate nature
of these theoretical predictions when applied to the present case. The
basis of the method is the assumption that the accelerator can be treated
as a thin lens (lens dimension is short compared with the focal length).
Further, the angle an ion makes with the axis of symmetry is assumed
small, so that the equations governing the spreading can be simplified
by "paraxial ray" assumptions. Thus, no allowance is made for space
charge effects in the accelerator region nor for the potential depression
at the emitter due to the aperture in the accelerator electrode. However,
experience reported on electron gun design (ref. 14) suggest that the
simple assumptions are adequate.

For all the measurements reported herein the acceleration system is
operated in an "accel-decel" mode. That is, the accelerating electrode is

operated negative with respect to ground and the plasma potential is assumed to return to near ground without a physically grounded electrode being used (ref. 12). No previous systematic study of the ion optical properties of a "virtual" decelerator or ground are available. Such data is desirable, since Kaufman, reference 15, finds that the use of a "virtual" electrode may have many practical advantages in actual space rockets. It seems reasonable to assume that the spatial position of a virtual decelerator will vary as a function both of the negative accelerator potential and the ion beam density. For small negative accelerator potentials, the beam spreads due to thin lens effect and the universal beam spread results, but deviations may be encountered when the emitter-accelerator voltage difference becomes appreciably greater (2 or more times) than the emitter voltage. The ion optical properties in the deceleration region are intimately connected with the space charge neutralization of the exit beam by electrons.

Three possible factors which may contribute to beam divergence are: (a) the slightly enlarged accelerator aperture, (b) the lens action of this aperture and (c) the space charge spreading of the exit beam. Sketch 1 shows the fixed angle spreading effects of (a) and (b). The focal length of the diverging aperture of the accelerator is

$$f_{aperture} = 5.72l \tag{10}$$

Spangenberg (ref. 13, p. 354) gives the following equation for a single-aperture lens

$$1/f_{len} = \frac{V'_o(z_2) - V'_o(z_1)}{4V_o(z_2)} \tag{11}$$

Plane of
hot wire
survey
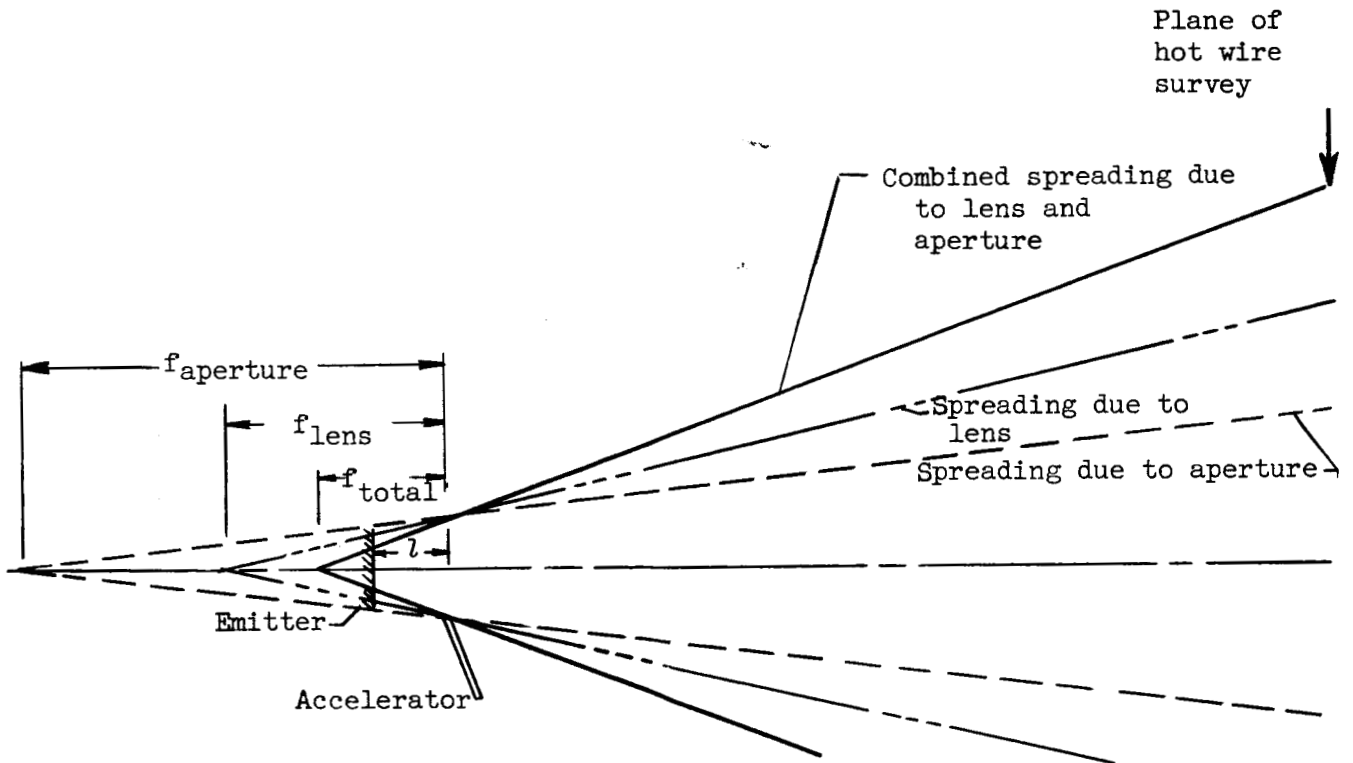
Sketch I. - Beam spreading.

where Z_1 refers to a point to the left of the lens just outside of the

region of appreciable potential variation and Z_2 refers to a corresponding

point to the right of the lens. For simplicity it is assumed that the

voltage $V_o(Z_2)$ remains constant beyond the accelerator, thus $V_o'(Z_2) = 0$.

$V_o(Z_2)$ corresponds to the voltage difference between emitter and ac-

celerator, therefore, the slope $V_o'(Z_1)$ is approximately $V_o(Z_2)/l$, and

the lens focal length is

$$f_{lens} = -4l \tag{12}$$

and the combined aperture and lens focal length is

$$1/f_{total} = 1/f_{aperture} + 1/f_{lens} \tag{13}$$

It is not certain that the oversized aperture will be important in the

beam spreading. However, the lens effect will definitely be a factor.

Spangenberg (ref. 13, p. 454) suggests that the addition of grid wires will not change the large aperture effect, but the individual holes in the grid will each have an action similar to that of the large aperture and with the same focal length.

The universal beam spread relations due to space charge has been developed in detail for electrons. Spangenberg has summarized the results necessary for predicting beam spreading into a single curve (ref. 13, p. 465). The parameter necessary to enter the curve to obtain radius increase of beam directly is

$$\frac{J^{1/2}}{V^{3/4}} \frac{Z}{r_o}$$

where Z is the distance downstream to the measuring station, r_o is the radius of the ion beam where the ion flow is originally parallel. J is the beam current and V is the beam voltage. From Child's law, equation (1) the beam current can be computed as

$$J^{1/2} = \left(\sqrt{4.75 \times 10^{-9} \times \pi} \right) \left(\frac{\Delta V^{3/4}}{l} \right) r_e \tag{14}$$

where r_e is the radius of the emitter. Equation (14), thus, leads to the necessary parameter for beam spreading as

$$\text{Constant} \times \left(\frac{\Delta V}{V} \right)^{3/4} \times \frac{r_e}{r_o} \times \frac{Z}{l} \tag{15}$$

For a fixed value of l/D the beam spread should be a function of $\Delta V/V$ only. That the beam spread is a function of $\Delta V/V$ was demonstrated in figure 18, where it was assumed that the net beam accelerating voltage is equal to the emitter voltage.

In figure 16 data taken with and without grid wire across the aperture are compared with different modes of beam spreading. In all cases, an allowance for aperture plus lens effect plus universal beam spreading overpredict the observed spread at the survey station. The sum of the spread due to lens action and the universal beam spread seems to approximate the data for the open aperture case and $\Delta V/V < 2$. In the case of the grid wire data, only the universal beam spreading was needed to fit the spread; however, it was necessary to use $r_0 = 0.50$ inch corresponding to the accelerator diameter in the universal beam spread relations. For the open aperture case, the emitter radius, $r_0 = 0.41$ inch correlated the data best. Above a $\Delta V/V$ of 2 the open aperture beam spreads at a rate much less than even the universal beam spreading predicts. Above a $\Delta V/V$ of 2, the magnitude of the accelerator voltage exceeds the magnitude of the positive emitter voltage. Here the effect of a virtual electrode to return the beam to ground potential is most pronounced. Several factors associated with the virtual "decelerator" may contribute to the lack of spread. First, a real "decelerating" aperture would generally have a focusing lens action (ref. 13), which might in part compensate for the defocusing at the accelerator. Perhaps of more importance, the large negative potential of the accelerator would tend to "push" the plane of the virtual decelerator further and further downstream. The effective length from the plane of the hot wire survey to the virtual decelerator is much shorter at the high potential than at the lower potentials. The data is too limited in the case of grid wires to tell much about the spreading beyond $\Delta V/V = 2$.

Beam neutralization. - If the beam is essentially neutralized downstream of the virtual decelerator then the beam would spread at a constant angle, determined by the radial velocity component at the plane of neutralization. This effect could in fact explain the lower spreading rate observed in figure 16(a) at the high voltage rates. However, the present ion beam is thin enough that it may extend for a great distance without neutralization.

No systematic program relating to beam neutralization has as yet been run with the present ion beam. A 0.005 inch diameter tantalum wire was mounted across the beam at a distance of 5.6 inches downstream of the emitter for all the runs reported. For most of the data reported the tantalum wire was heated only slightly and operated at essentially ground potential. Typical surveys across the ion beam with different degrees of electron emission from the tantalum wire are shown in figure 17. The major effect observed by the hot wire calorimeter in figure 17 is the increase in thermal radiation obtained from the hot tantalum wire. The hot-wire, which surveys a plane 1.5 inches downstream of the neutralizer wire, travels at a right angle to the neutralizer. The location of the neutralizer wire may be noted on figure 17 by the blip caused by the shadow of the wire near the centerline of the survey. Some evidence of a local increase in power density is occasionally observed near the neutralizer wire.

Internal secondary electrons. - Efficient ion rocket designs will require maximum acceleration of ions with minimum interference. The design of an accelerator with no ion impingement is the aim of several

current research projects. The Pierce accelerator system offers an analytical technique for obtaining the ideal conditions at the design point. However, future operation will require off as well as on-design performance from a given accelerator. The present evaluation has yielded several interesting observations in regard to accelerator impingement.

Some impingement and sputtering is encountered on the accelerator in all the runs reported. With accurate alignment the impingement appears to follow a trend indicated by figure 18(a). The sharp minimum in percent impingement occurs at approximately the design point of space charge limited flow. The minimum is bounded by a reduction in accelerator impingement for less than space charge limited flow, and a more gradual decrease at the higher neutral cesium flow rates. The region of vaporizer temperatures just below the minimum is a highly unstable operating condition for the system.

Figure 18(a) shows the effect of impingement for two different emitter temperatures. Figure 18(b) further shows the effect of emitter temperature on accelerator impingement at a fixed vaporizer temperature in the space charge limited flow region. Figure 19 shows the hot wire surveys corresponding to the impingement measurements of figure 18(b). The increase in impingement with emitter temperature might be explained as due to the increased thermal velocity of the emitted ions. However, a striking change occurs in the power distribution curves of figure 19, when the impingements begins to rise sharply. Instead of thermal velocities causing a noticeable effect on overall beam shape, local maximums in power density start to appear. The power contained within the local peaks was found to correlate well with the increase in emitter

current. However, the overall addition in power as computed from the
hot wire surveys is not greatly affected by the local maximums. The
increase in emitter current was thought to be due to secondary electrons
caused by the accelerator sputtering. This lead to the speculation that
the local maximums were in some way related to the ion impingement on the
accelerator.

The hot wire indicates only the power contained in the beam. No
distinction can be made between ions or electrons of equal energy.
Therefore, indirect observations were required to infer that the local
maximums are due to ions. Figure 20 shows a typical accelerator with
grid wires after operation in the ion beam. In all cases it was found
that a region of high sputtering occurred in a circle smaller in diameter
than the accelerator aperture. The region of maximum sputtering appears
to correspond to the local maximums in power density observed downstream
(fig. 19). It seems almost impossible that electrons could ever strike
the grid wires, since they are at high negative potential. Thus, it is
concluded that the local maximums in power density must be due to positive
ions.

A further bit of information relating to the problem is shown in
figure 21. When the non-Pierce grid wire accelerator was operated, no
local maximums corresponding to figure 19 were observed. In figure 21
a typical sputtered grid wire is shown. No accelerator edge was present
in this case, so the maximum sputtering is over the entire center region
of the wire and not at the edges. The run conditions are different for
the different accelerators, therefore, the exact role of the accelerator
lip in producing the local power maximums can not as yet be definitely
established.

A possible improvement of the accelerator. - The observation of
local maximums in ion beam power density has led to the experimental
testing of a possible means of improving ion acceleration. Although the
mechanism producing the local beam power increase is not known, it is
believed to be directly connected with secondary electrons caused by the
accelerator sputtering. It is thought that the sputtered material has
in some way affected the local space charge distribution within the
accelerator system. With these thoughts in mind a controllable electron
emitter was mounted in the region between the ion emitter and the ac-
celerator. Figure 22 is a photograph of a thoriated-tungsten wire
electron emitter mounted on the beam forming electrode. The circle of
wire is insulated from the electrode and sets about 0.15 inch above the
ion emitter. The accelerator was mounted 0.82 inch away from the ion
emitter (L/D = 1.0). During operation the voltage of the electron
emitter is set at approximately the corresponding space charge voltage
existing at 0.15 inch above the ion emitter (this potential was usually
within a few hundred volts of the positive ion emitter potential). The
thoriated wire is heated to boil off electrons, which should in turn
fall to the ion emitter (since the accelerator is operating at a high
negative potential, no electrons would escape in that direction) and
give rise to locally sputtered secondary electrons. It was hoped that
this configuration might approximate the conditions occurring in the
accelerator sputtering case, but with external control on the electron
emission. The thoriated wire loop was 0.57 inch in diameter to insure
the electrons are in the region of the beam.

Figure 23 demonstrates the results obtained with the thoriated-tungsten-electron emitter. On the left of figure 23 typical beam profiles obtained up to space charge limited conditions are shown. The right side profiles show the effect obtained with the internal electron emitter operating. Figure 24(a) shows the corresponding total power measurements computed from the profiles. There is no doubt that the electron emitter greatly increases the ion beam power. However, it is uncertain whether the increase in power brought about by the emitter is due to the same mechanism that produced the local peaks observed in figure 19. Figure 24(b) shows the three highest current points obtained to date with the internal electron emitter-accelerator system. The highest point corresponds to an increase of 25 times over that of Child's law.

It is impossible to prove that the increased power is due to ions only from the data at hand. However, it does not seem reasonable that the vaporizer limited values of power would follow the normal curve (fig. 24(a)) if high energy electrons were causing the great increase in power. It would appear that if high energy electrons were causing the observed increase in calorimeter power they would be unaffected by vaporizer temperature.

The present accelerator configuration represents a first attempt to augment the Pierce accelerator system. It appears to have lead to much larger gains in ion current than electrical space charge limitation will allow. The present augmented accelerator results in no way represents the maximum power that even the present ion rocket might be made to produce.

Thus, it might be expected that large gains, over the Pierce acceleration system, can be made in the acceleration of ions.

CONCLUSIONS

The present report outlines the steps taken to evaluate the production and accelerations of ions. A porous tungsten ion source and a Pierce accelerator system similar in principle to proposed space propulsion systems is studied in detail. It is demonstrated that cold flow calibrations of the porous tungsten leads to accurate predictions of its ion production properties. Both the maximum current and critical emitter temperature obtained experimentally are shown to agree well with theoretical predictions.

Previous data on the evaporation of cesium from tungsten leads to the prediction of a hysteresis loop in critical emitter temperature. This hysteresis loop in critical emitter temperature is experimentally demonstrated.

The effect of aperture in the Pierce accelerator is investigated. It is demonstrated that the use of grid wires across the aperture to eliminate the potential gradient across the ion emitter improves the agreement of total ion power with the predictions of Childs' law.

An investigation of beam spreading for "thin" beams indicates that with an open aperture, the beam spreads due to space charge and a lens action for $\Delta V/V < 2$. At large accelerator voltage the spreading is much less than is predicted by even space charge spreading alone. With grid wires the beam spread can be attributed to space charge spreading alone.

Observations of unexpected local maximums in beam power distribution were traced to impingement of the ion beam on the accelerator. These local

maximums suggested that the use of an external source of electrons between the ion emitter and accelerator would increase beam power. A thoriated-tungsten wire electron emitter between the ion emitter and the accelerator was found to greatly increase the total power available from the basic Pierce accelerator.

REFERENCES

1. Stuhlinger, E.: Possibilities of Electrical Space Ship Propulsion. Extract from Proc. Fifth Int. Astronautics Cong., 1959, pp. 100-109.

2. Moeckel, W. E.: Propulsion Methods in Astronautics. Int. Ser. on Aero. Sci. and Space Flight. Vol. 2, Pergamon Press, 1959, pp. 1078-1097.

3. Baldwin, L. V., and Sandborn, V. A.: Theory and Application of Hot-Wire Calorimeter for Measurement of Ion Beam Power. Progress in Astronautics and Rocketry, vol. 5, Electrostatic Propulsion, Academic Press, pp. 425-446, 1961.

4. Baldwin, L. V., and Sandborn, V. A.: Hot-Wire Calorimetry: Theory and Application to Ion Rocket Research. NASA TR R-98, 1961.

5. Daykin, P. N.: Electrode Shapes for a Cylindrical Electron Beam. British Jour. of Applied Physics, vol. 6, pp. 248-250, 1955.

6. Pierce, J. R.: Theory and Design of Electron Beams. Second ed., D. Van Nostrand Co., N. Y., 1954.

7. Lockwood, David L., Mickelsen, William R., and Hamza, Vladimir: Application of Space-Charge Flow Theory to Electrostatic Rocket Engine Design. Proposed NASA TR.

8. Reynolds, Thaine W., and Kreps, Lawrence W.: Gas Flow, Emittance, and Ion Current Capabilities of Porous Tungsten. NASA TN D-871, 1961.

9. Taylor, John Bradshaw, and Langmuir, Irving: The Evaporation of
    Atoms, Ions, and Electrons from Caesium Films on Tungsten. Phys.
    Rev., Vol. 44, No. 6, Sept. 15, 1933, pp. 423-458.

10. Reynolds, Thaine W., and Childs, J. Howard: A Graphical Method for
    Estimating Ion-Rocket Performance. NASA TN D-466, 1960.

11. Brewer, G.: Applied Physics, 28, no. 1, Jan. 1957, pp.7-16.

12. Kaufman, H. R.: An Ion Rocket With an Electron-Bombardment Ion
    Source. NASA TN Dσ585, 1961。

13. Spangenberg, Karl R.: Vacuum Tubes McGraw-Hill, New York, 1948.

14. Baldwin, G. C.: Design of a 0-50-6 Kv Ion Accelerator-Decelerator
    for Propulsion. General Electric Report. TIS 59GL153, June 1959.

15. Kaufman, H. R.: One-Dimensional Analysis of Ion Rockets. NASA TN
    D-261, March 1960.

16. Honig, R. E.: Pressure Data for the More Common Elements. RCA
    Review, Vol. XVIII, no. 2, June 1957。
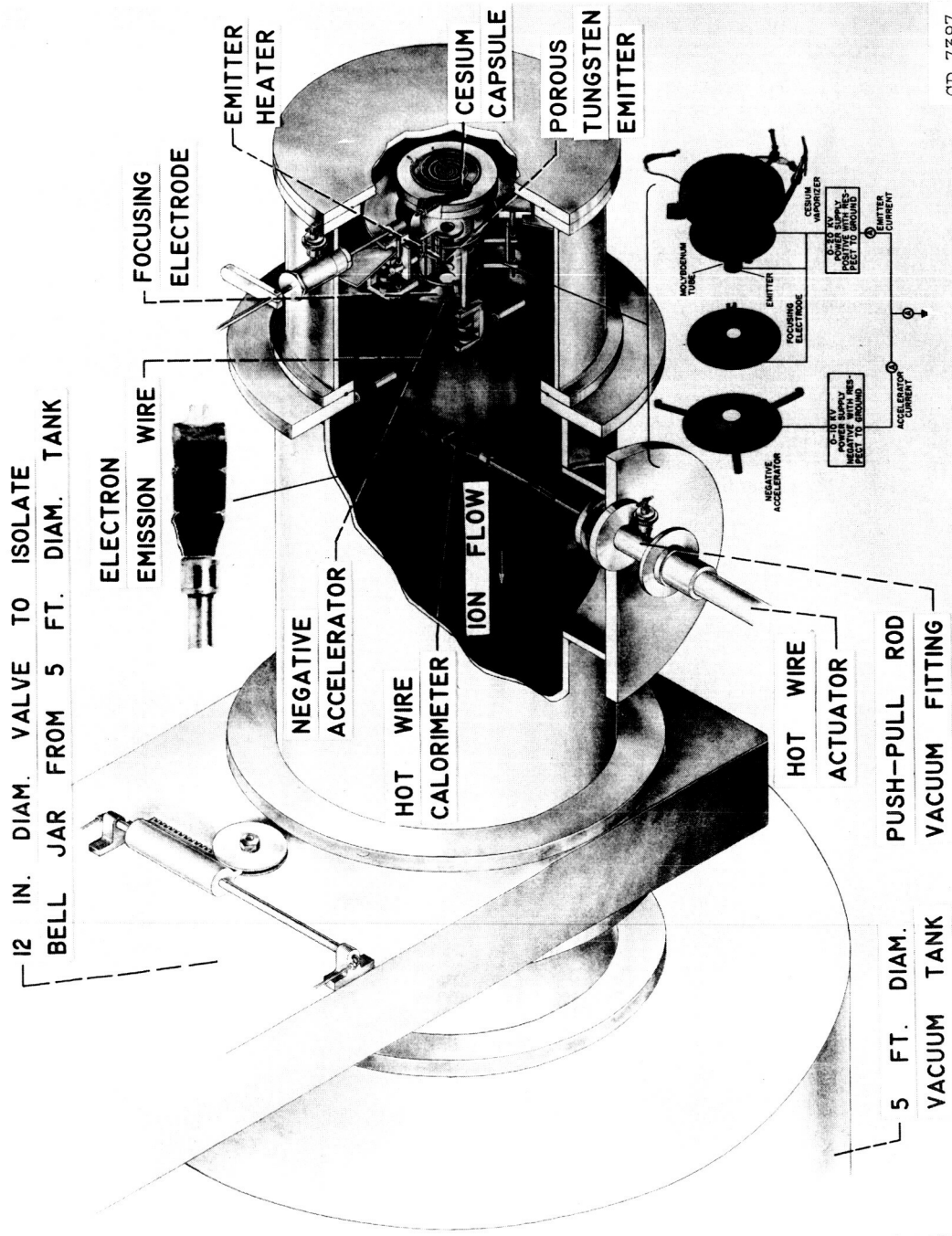
(a) Installation in vacuum facility.

Figure 1. - Sketch of test setup.

MOLYBDENUM TUBE
EMITTER
FOCUSING ELECTRODE

AIR
COOLING
TUBES

CESIUM VAPORIZER

ACCELERATOR

C-57637

0-10 KV
POWER SUPPLY
NEGATIVE WITH
RESPECT TO
GROUND

0-20 KV
POWER SUPPLY
POSITIVE WITH
RESPECT TO
GROUND

ACCELERATOR CURRENT (A)

(A) EMITTER CURRENT

COMMON (A)
GROUND
CURRENT
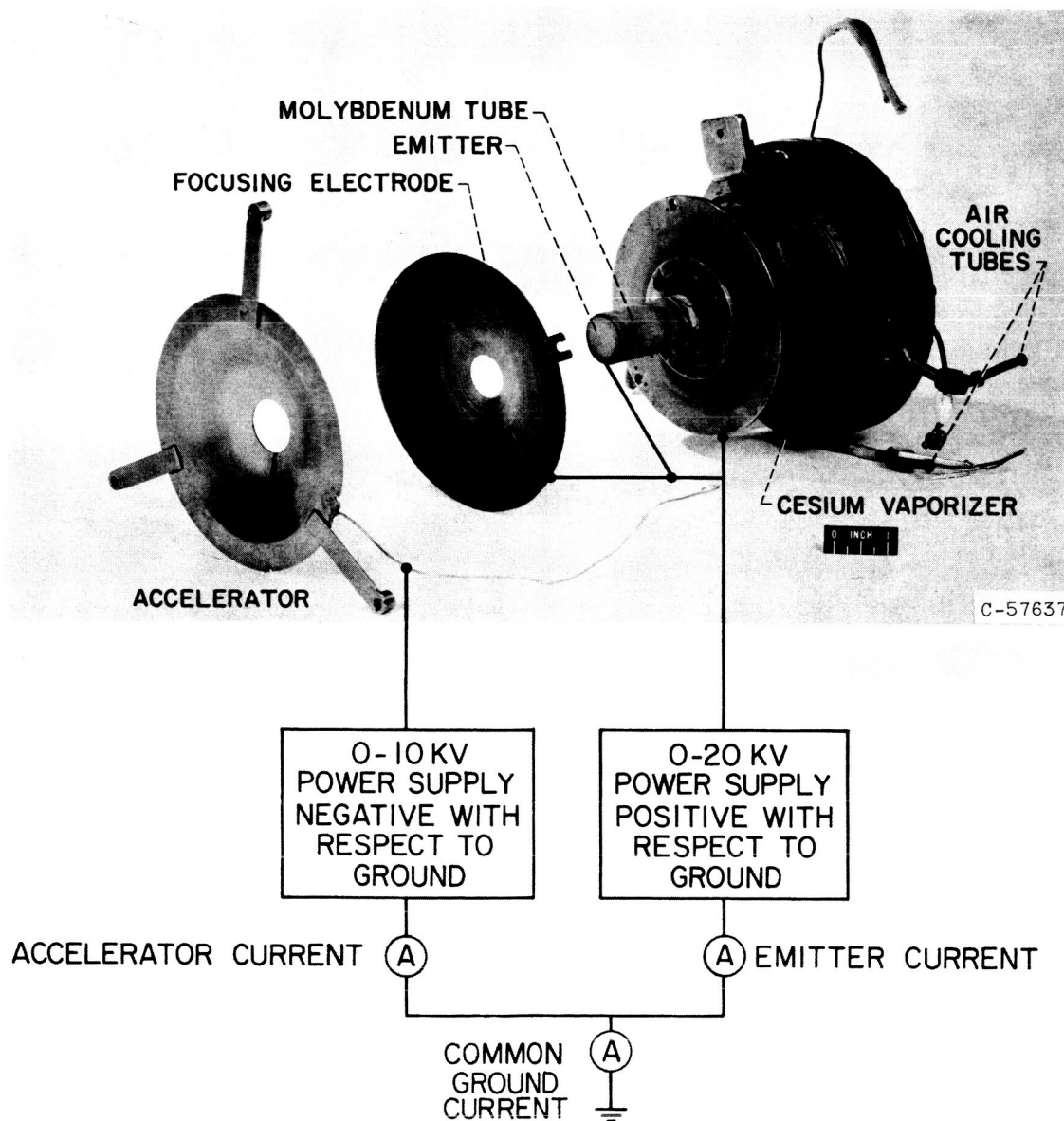
(b) Details of the engine.

Figure 1. - Concluded. The ion engine.

LOCATION
OF HOT
WIRE

COOLING
WATER IN

MICA SHIELD

OUT
COOLING WATER

PROBE
NO. 1

0 INCH

DIRECTION OF
TRAVERSE (ION BEAM
PERPENDICULAR TO
PLANE OF PHOTOGRAPH)

C-57639
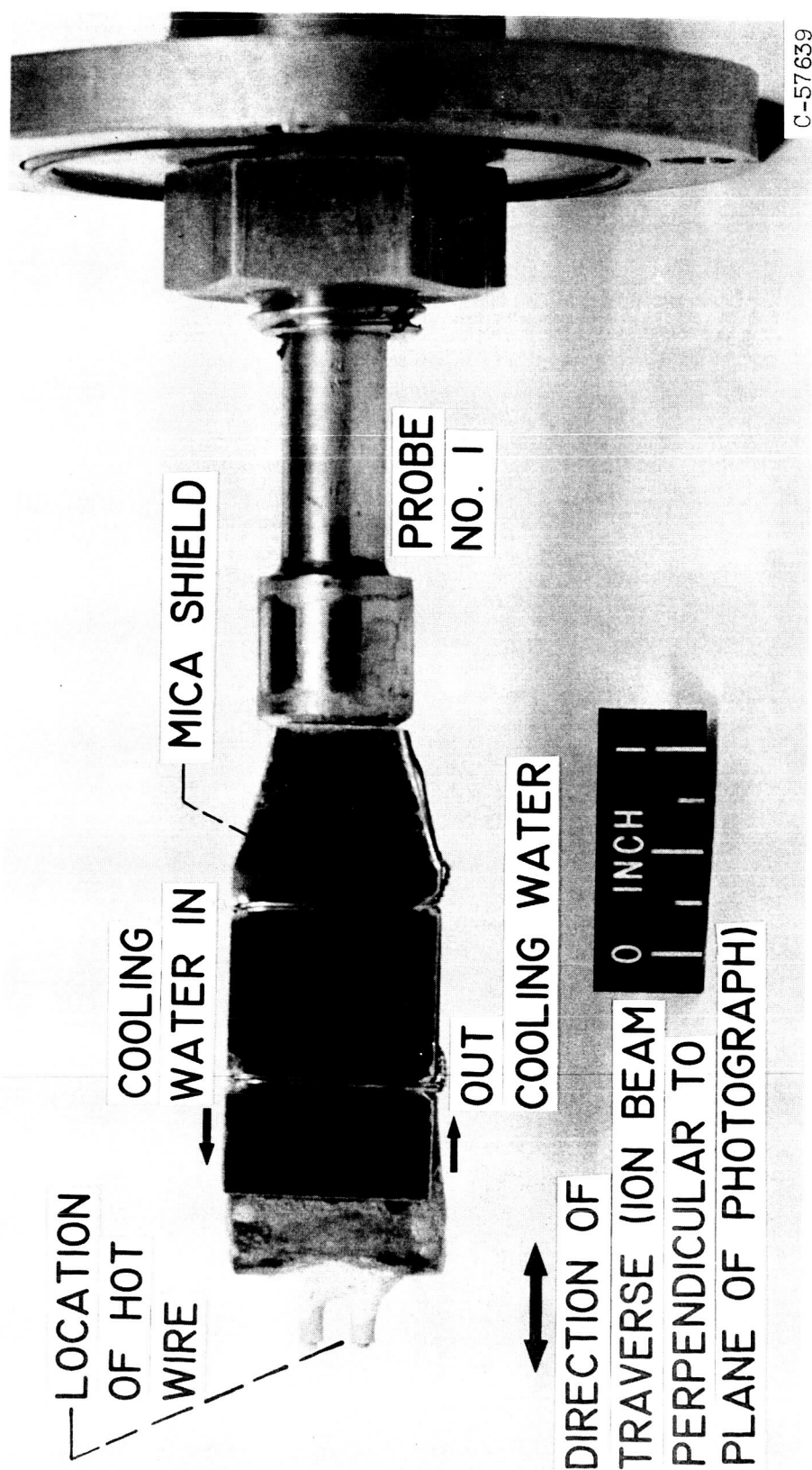
Figure 2. - The hot wire calorimeter probes.
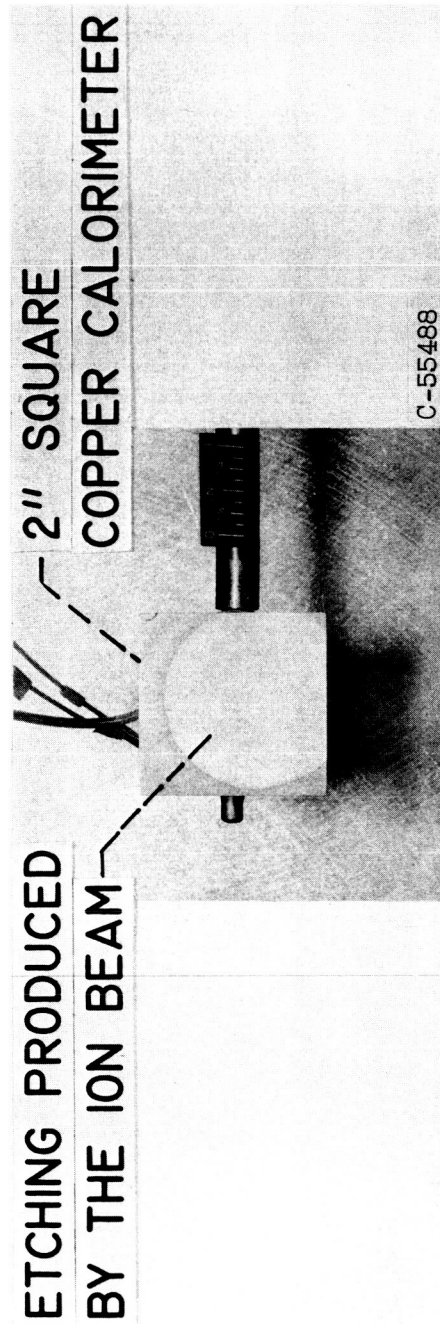
Figure 3. - Photograph of etching produced by the
ion beam on the calorimeter.

BASE LINE SHIFT DUE TO THERMAL RADIATION AND SUPPORT HEATING

ION BEAM POWER, DENSITY WATTS/FT².

DISTANCE FROM ENGINE CENTER LINE, IN.

(a) OPEN APERTURE ACCELERATOR. $T_{VAP.}$ = 425° F

ION BEAM POWER, DENSITY WATTS/FT².

DISTANCE FROM ENGINE CENTERLINE, IN.

(b) GRID WIRES ACROSS ACCELERATOR APERTURE. $T_{VAP.}$ = 400° F
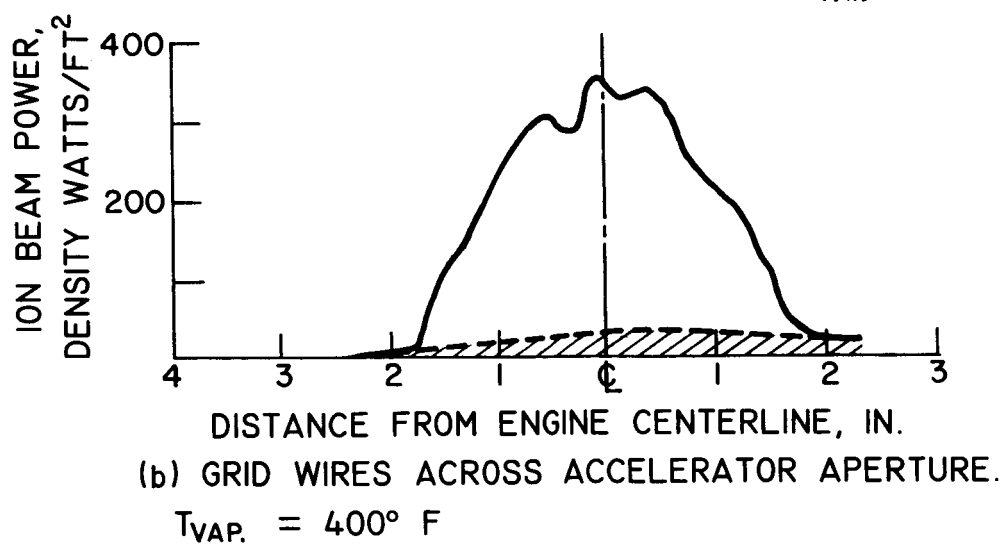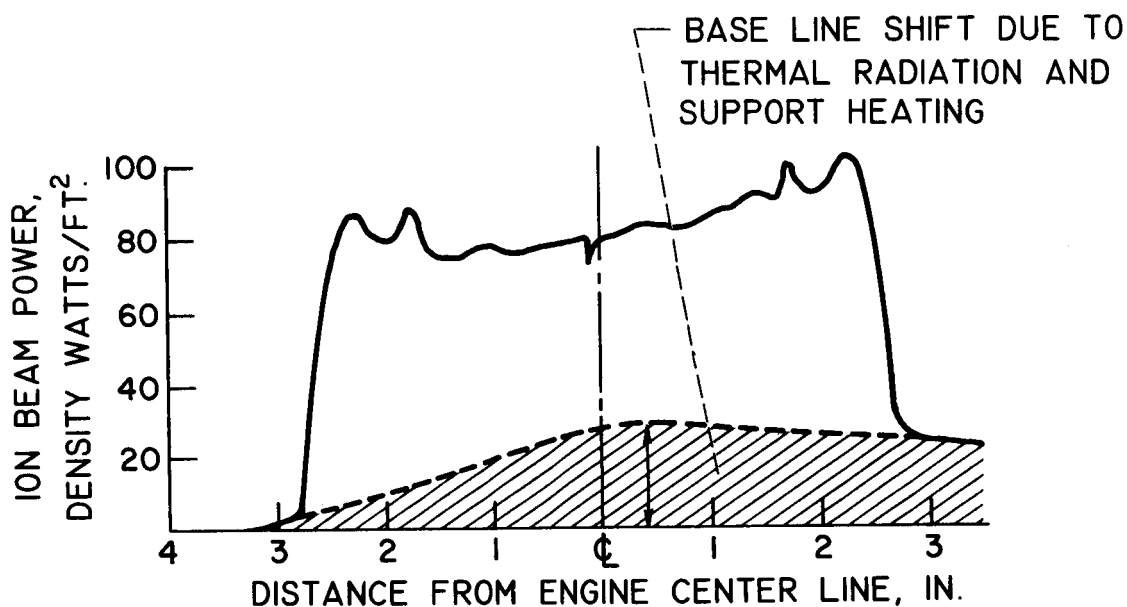
Figure 4. - Typical hot wire calorimeter traces. l/D = 0.87, emitter at +5 KV, accelerator at - 2 KV.
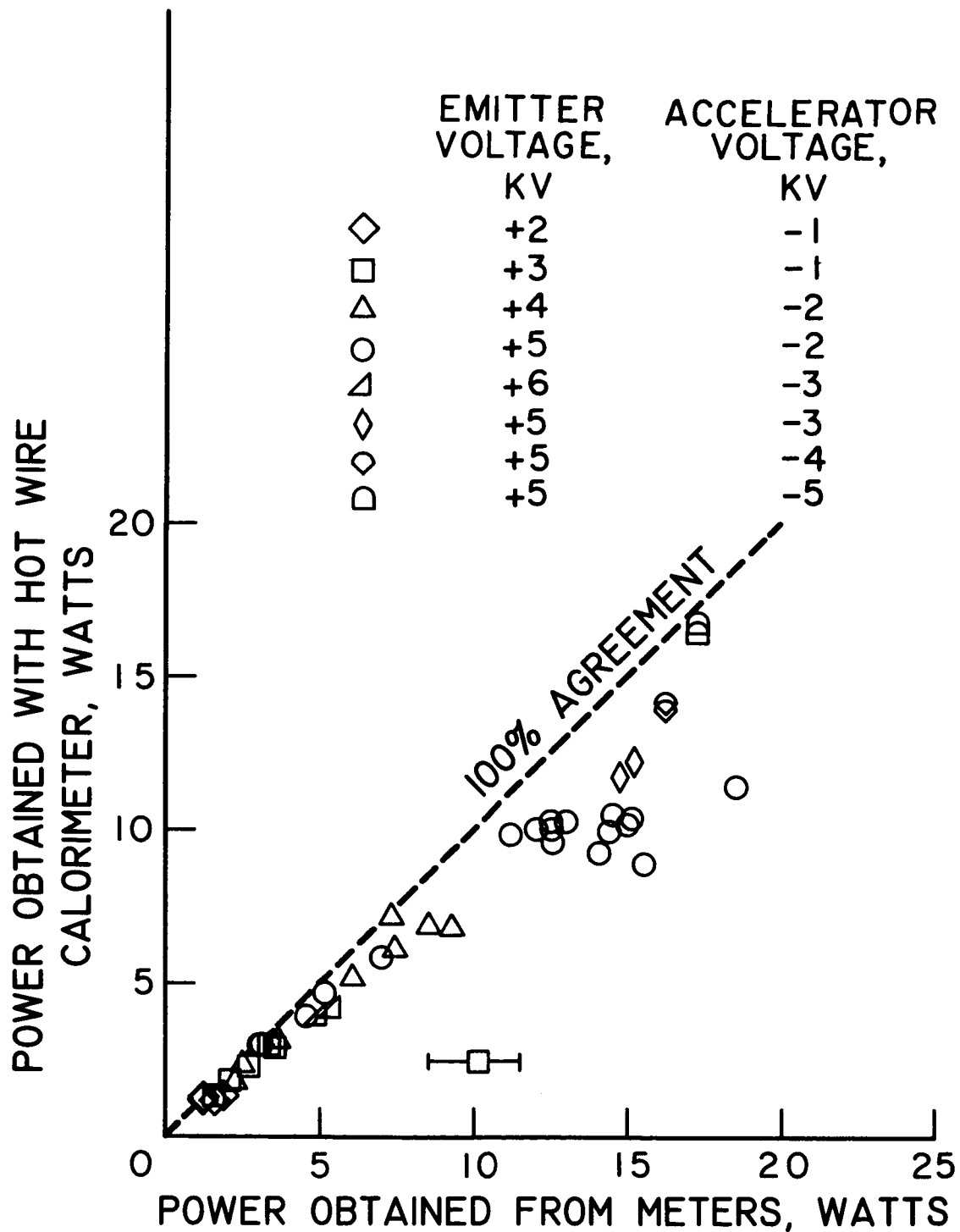
Figure 5. - Typical comparison between metered and hot wire measured beam power. l/D = 0.87, no grid wires.
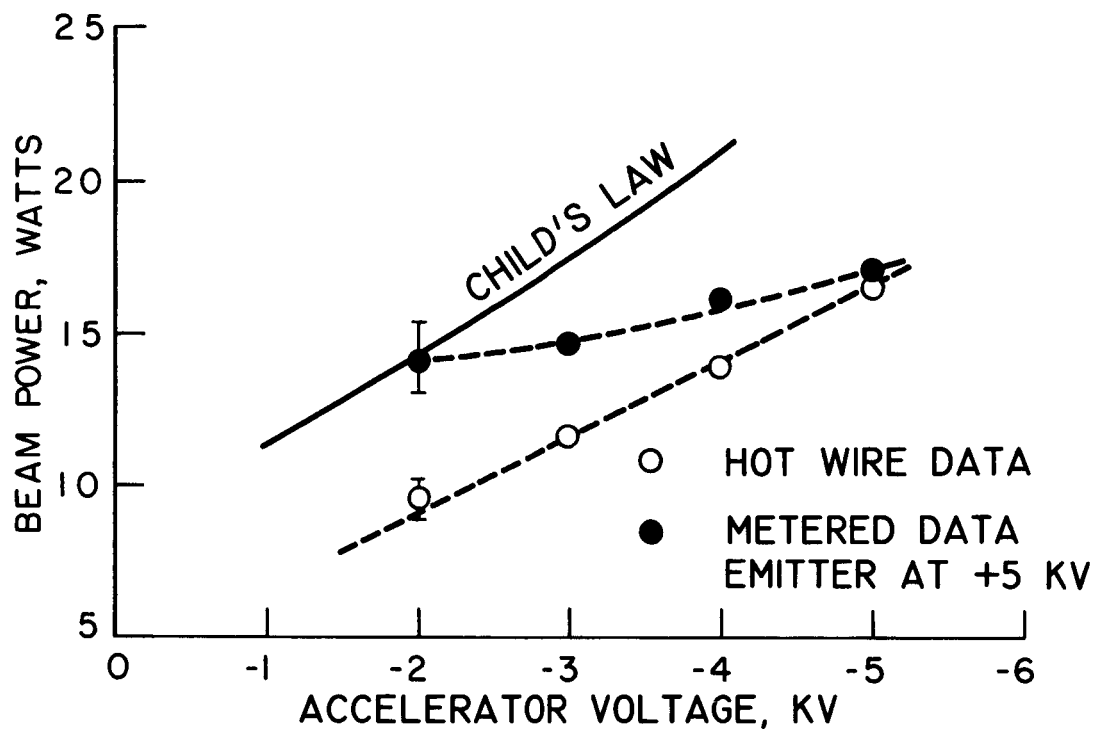
(a) SPACE CHARGE LIMITED OPERATION.
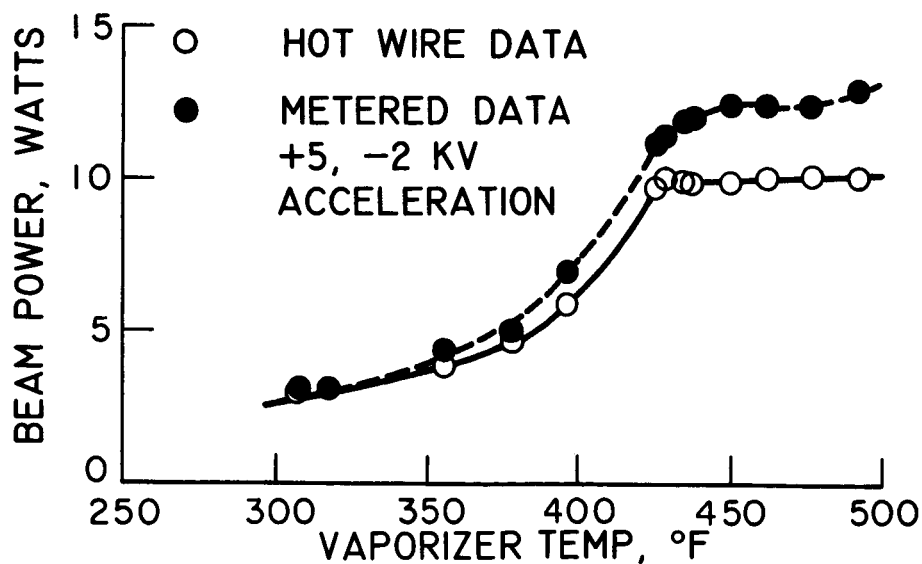
(b) VAPORIZER TEMPERATURE LIMITED OPERATION.

Figure 6. - Effect of external electrons on metered beam power. $\ell/D = 0.87$.
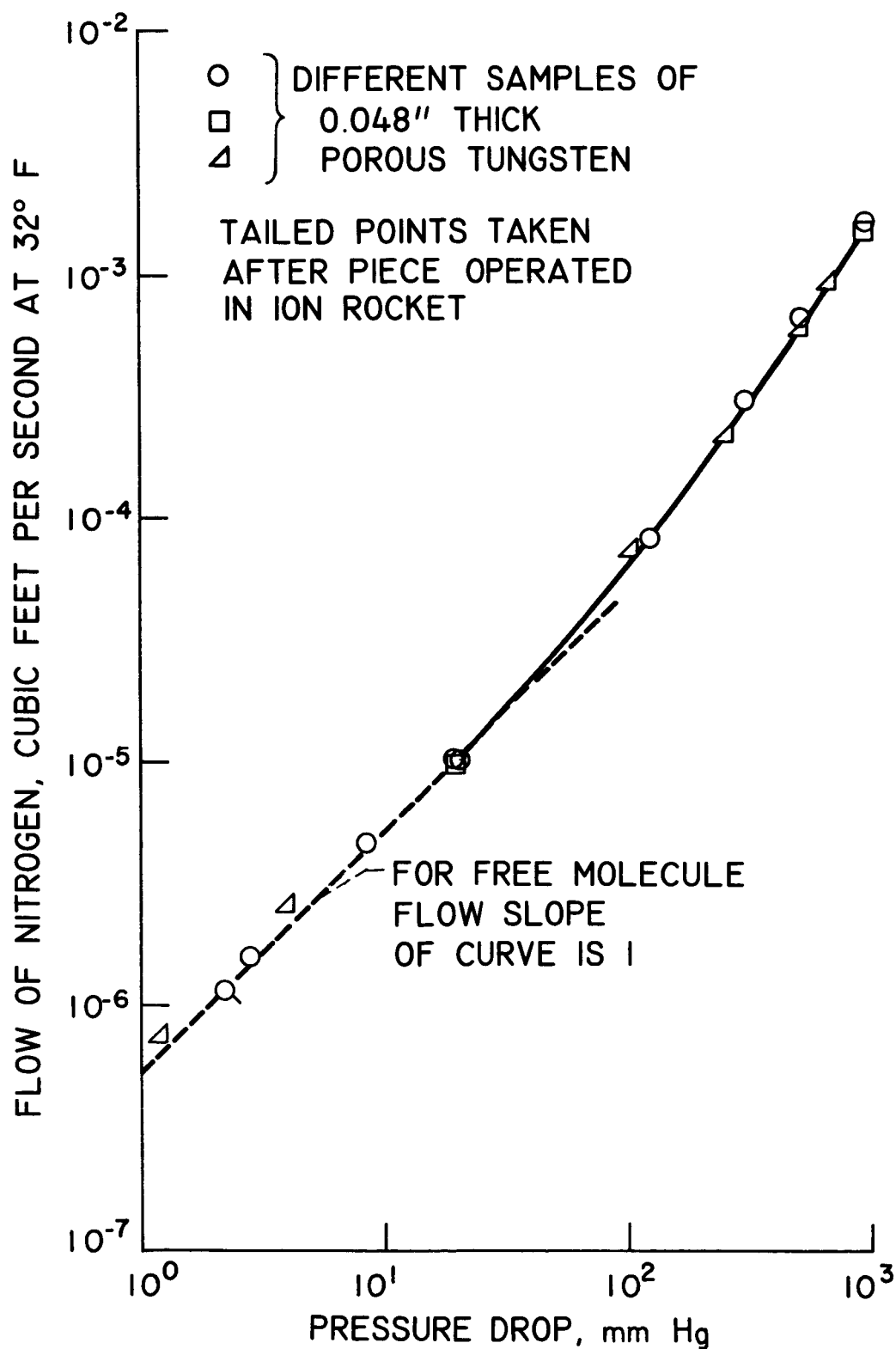
Figure 7. - Cold flow calibration of the porous tungsten emitters.
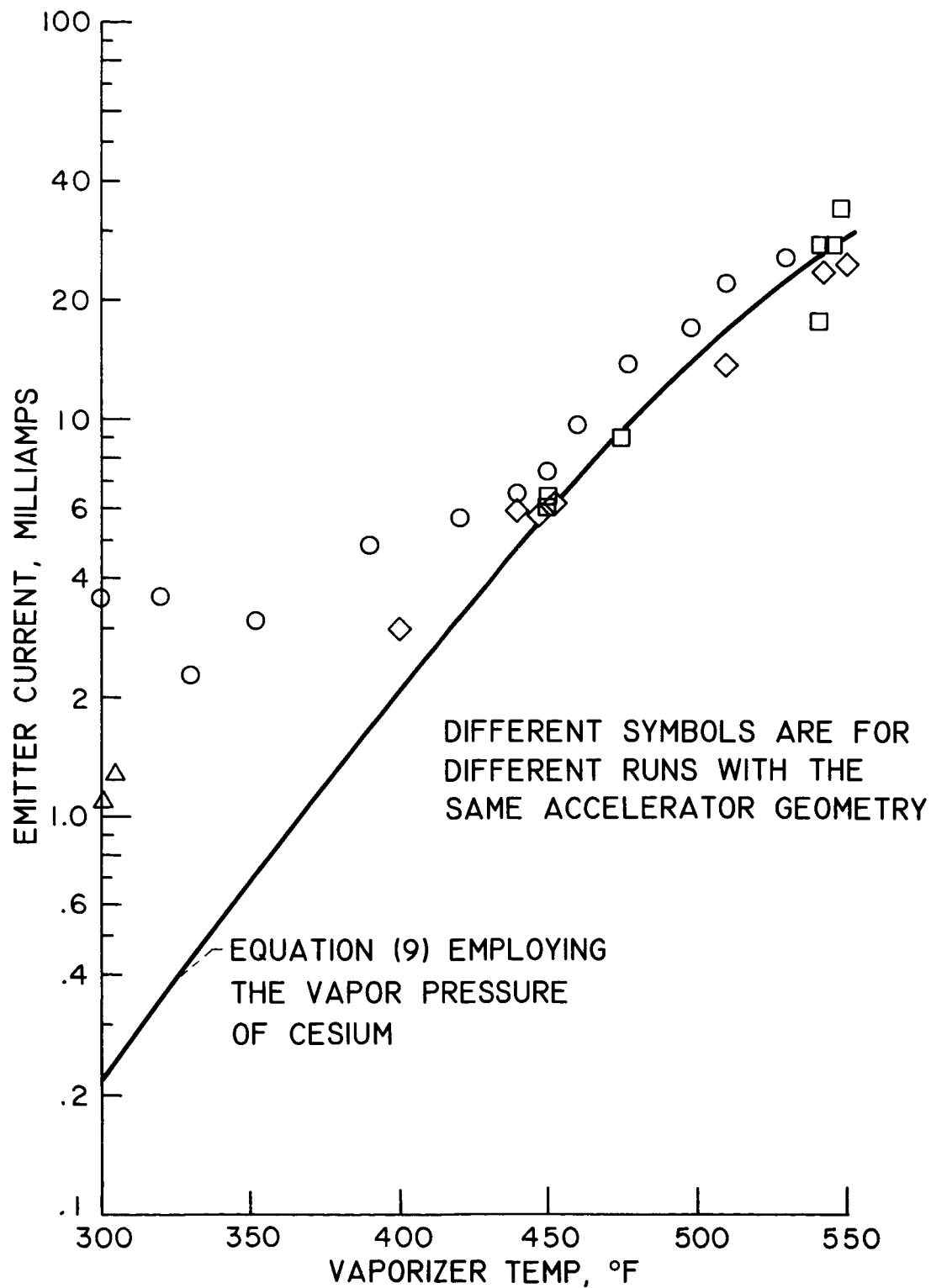
Figure 8. - Predicted and experimental emitter current as a
function of vaporizer temperature.
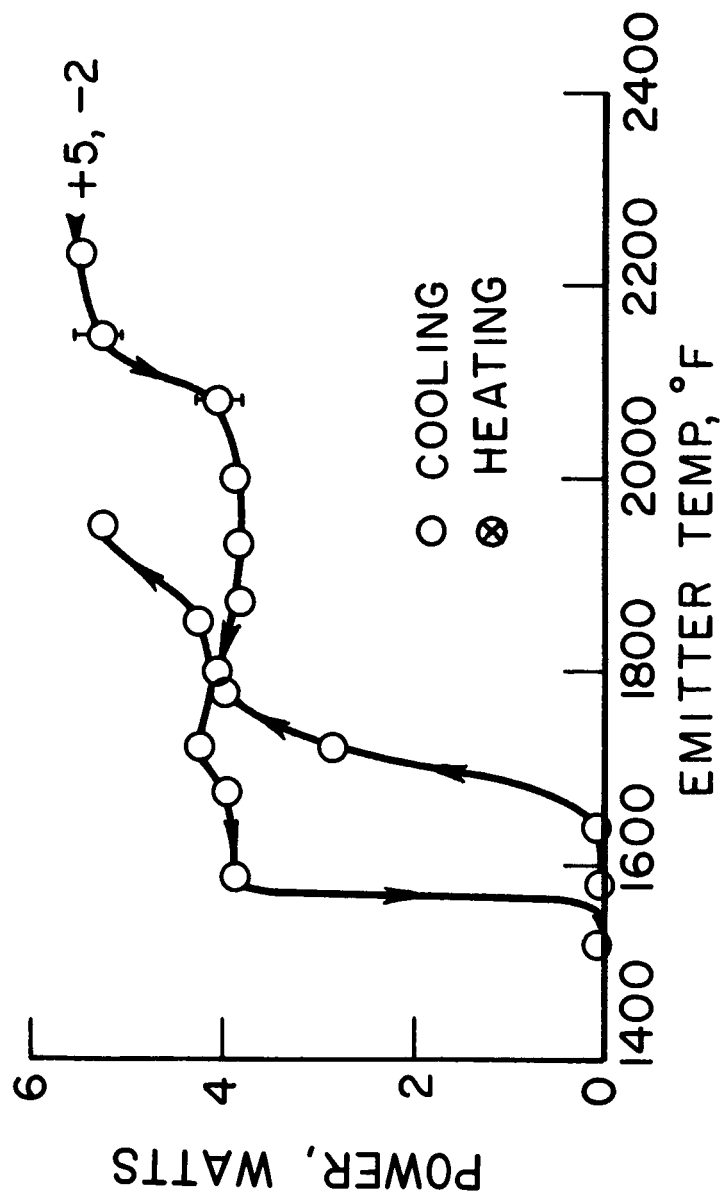
Figure 9. - Beam power variation with emitter temperature.

CURVE FOR CONSTANT ARRIVAL
RATE OF CESIUM 10^{16}
PARTICLES/CM^2 SEC

FRACTION OF MONOLAYER ABSORBED ON SURFACE

.16

.12

.08

.04

0.

CRITICAL
TEMP
POINTS

IONS

ATOMS

E D C B A F G H I J

ION PRODUCTION

HYSTERESIS
LOOP IN
ION
PRODUCTION

2200   2250   2300   2350   2400
TUNGSTEN EMITTER TEMP
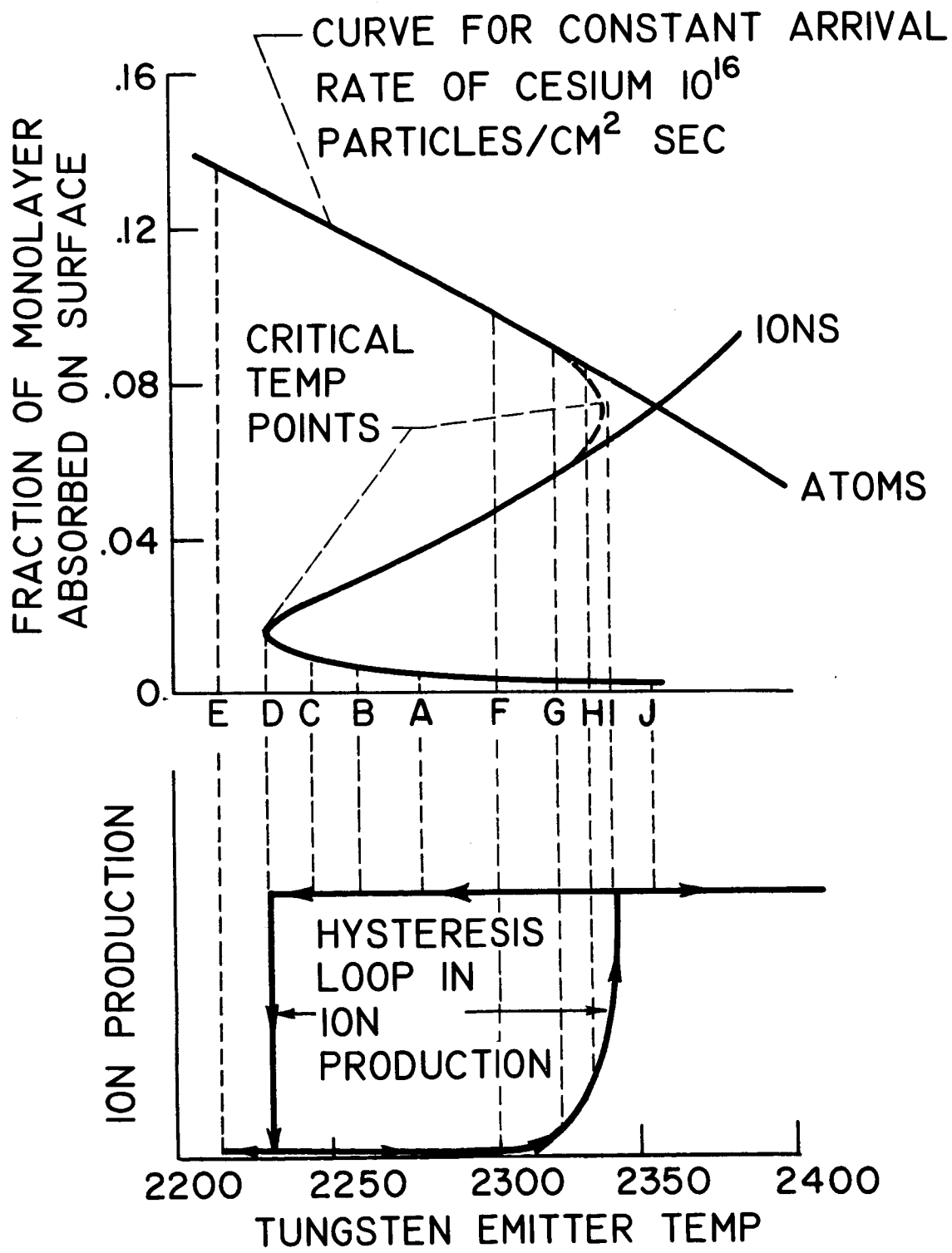
Figure 10. - Ion production hysteresis loop pre-
dicted from Taylor and Langmuir's data on the
evaporation of cesium from tungsten.
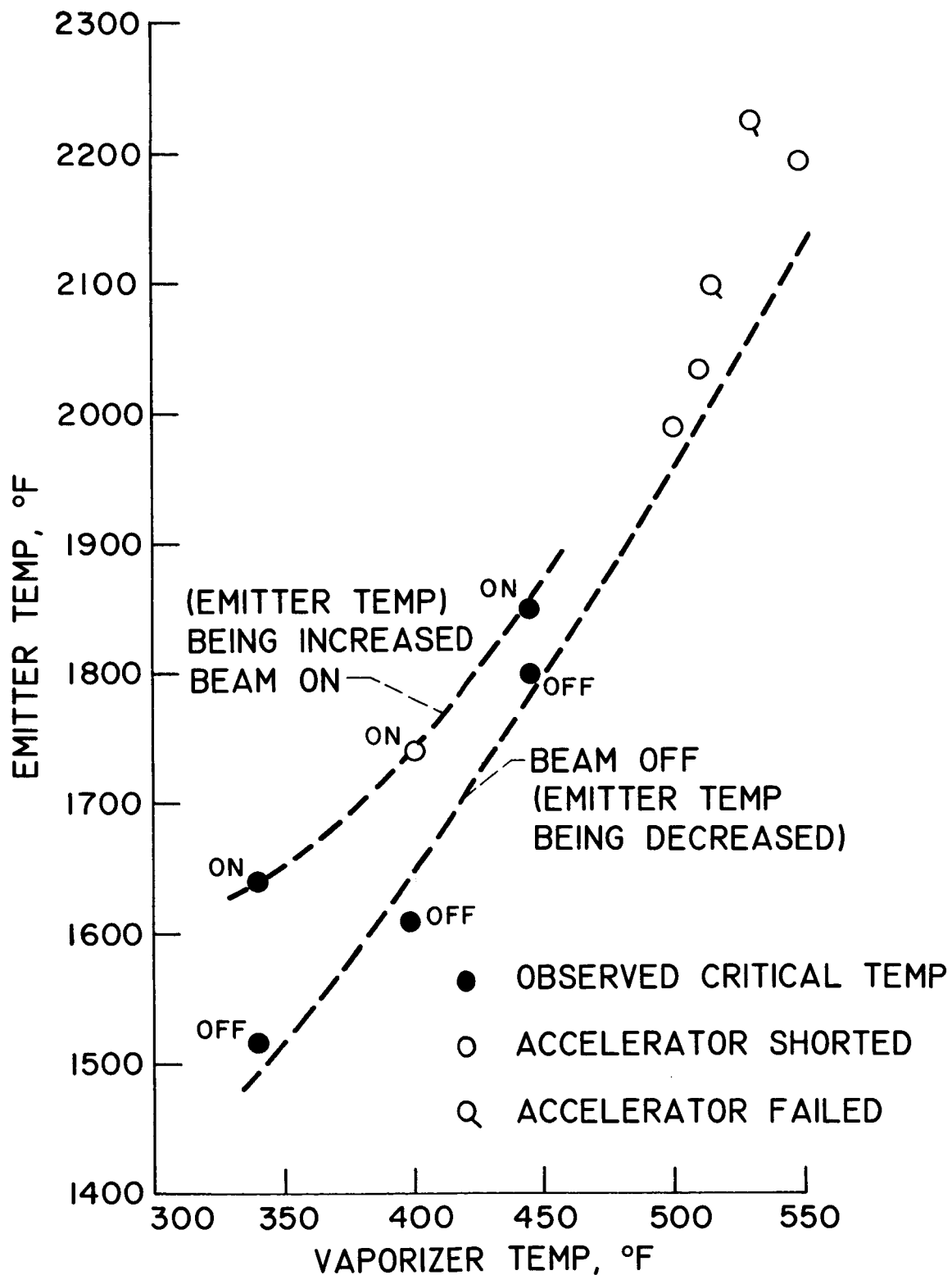
Figure 11. - Critical emitter temperature as a function of vaporizer temperature.
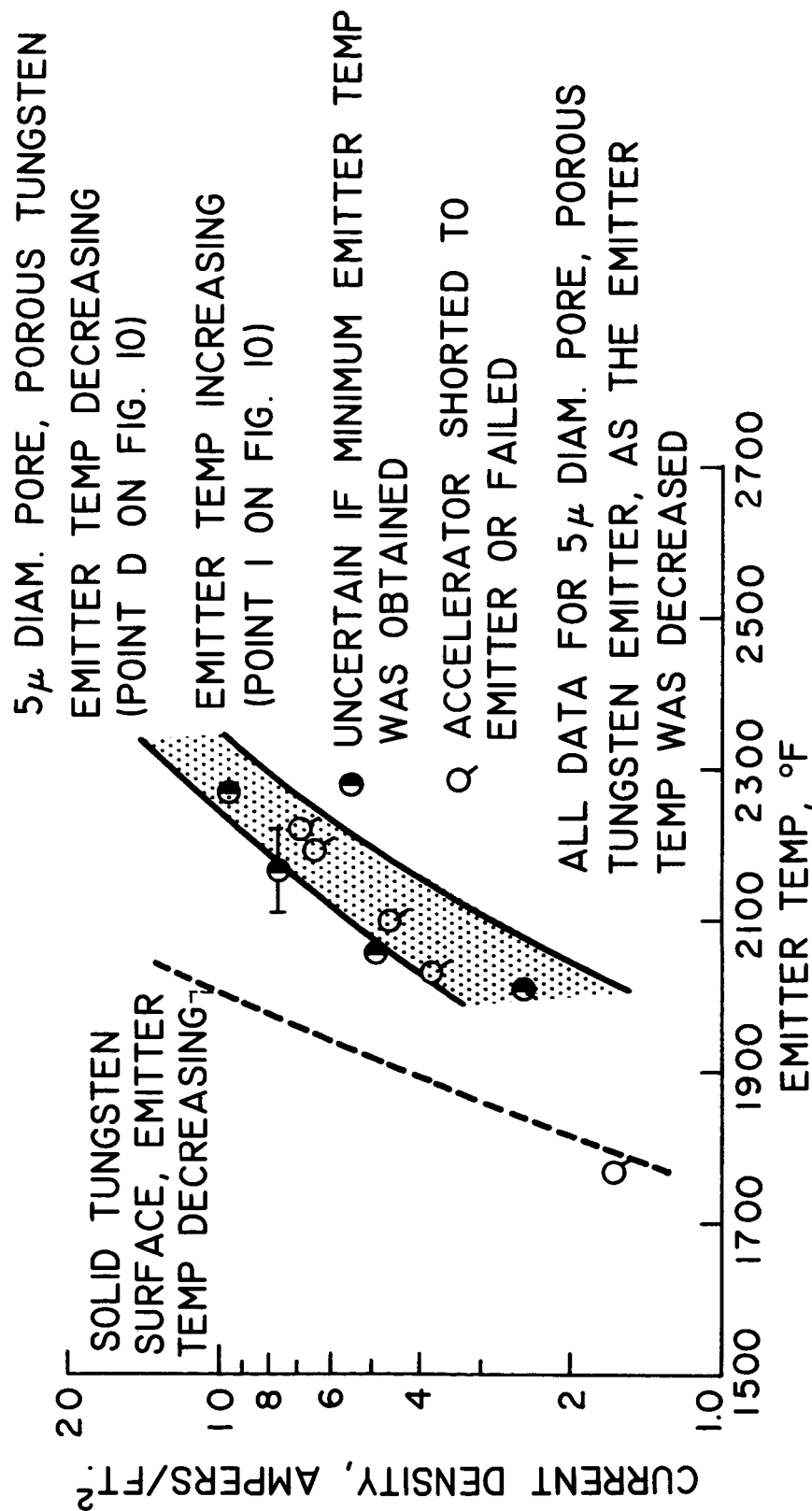
Figure 12. - Comparison of observed maximum current density at different emitter temperatures with analysis of Reynolds, ref. 8.
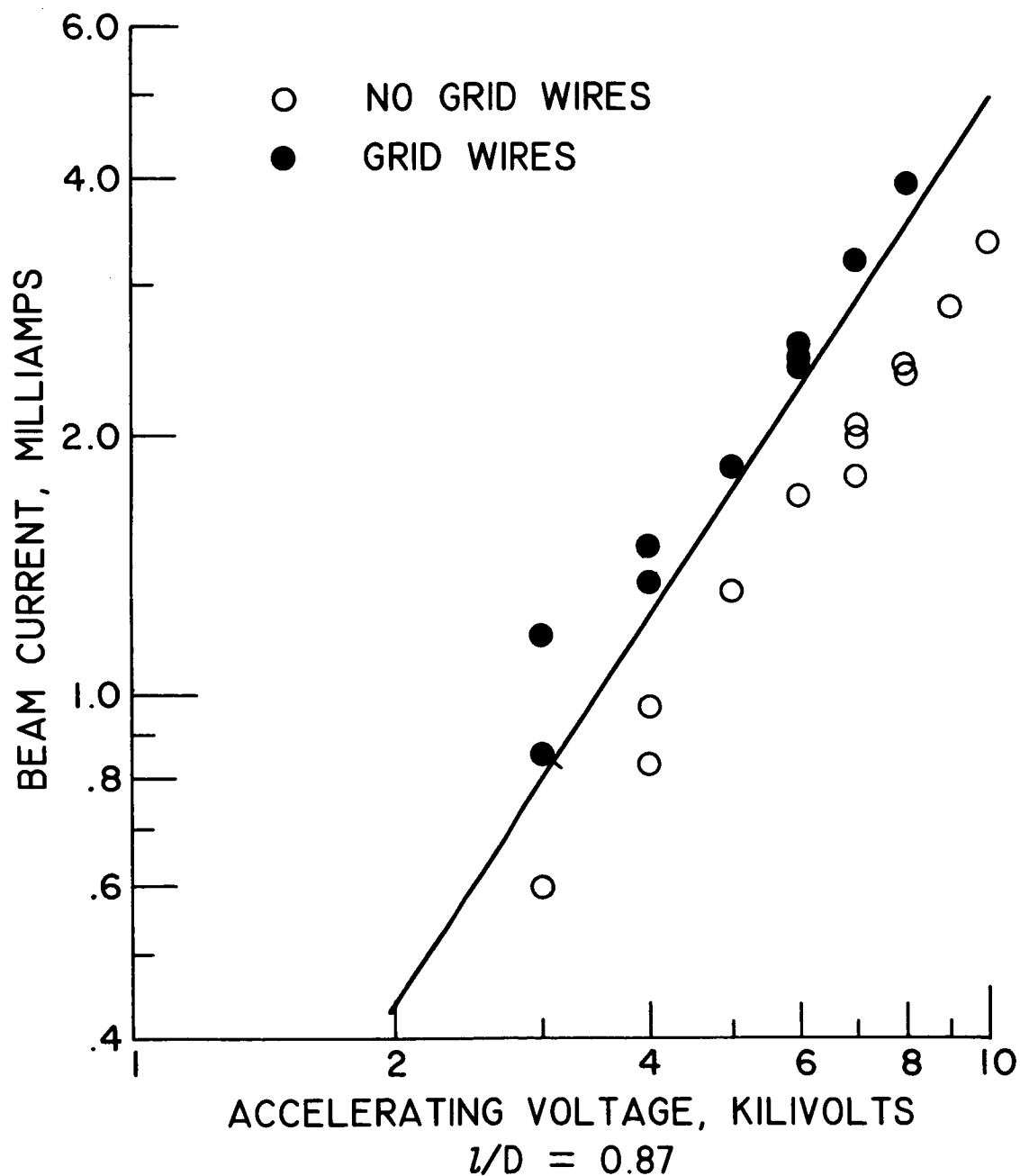
Figure 13. - Comparison of measured space charge beam current with Child's law.
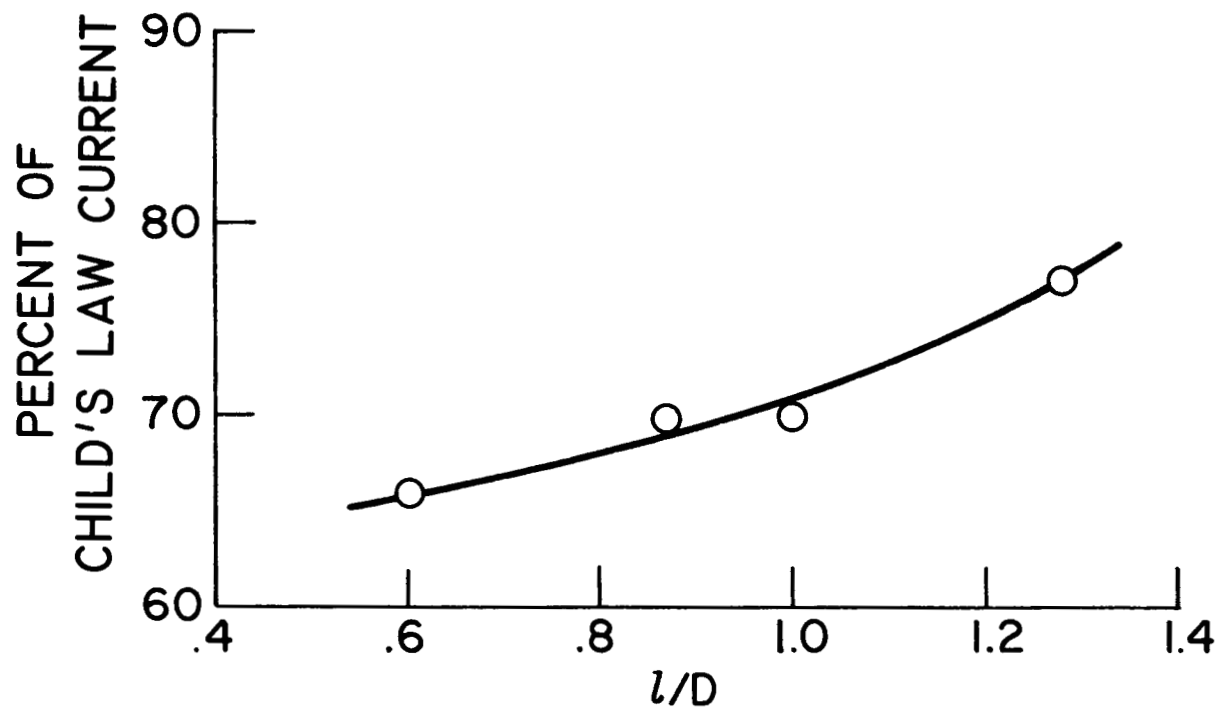
Figure 14. - Summary of aperture effect on beam current.

EMITTER	ACCELERATOR
VOLTAGE,	VOLTAGE,
◇ 2 KV	-1 KV
□ 3 KV	-1 KV
△ 4 KV	-2 KV
○ 5 KV	-2 KV

(a) OPEN APERTURE ACCELERATOR.

(b) GRID WIRES ACROSS THE ACCELERATOR APERTURE.
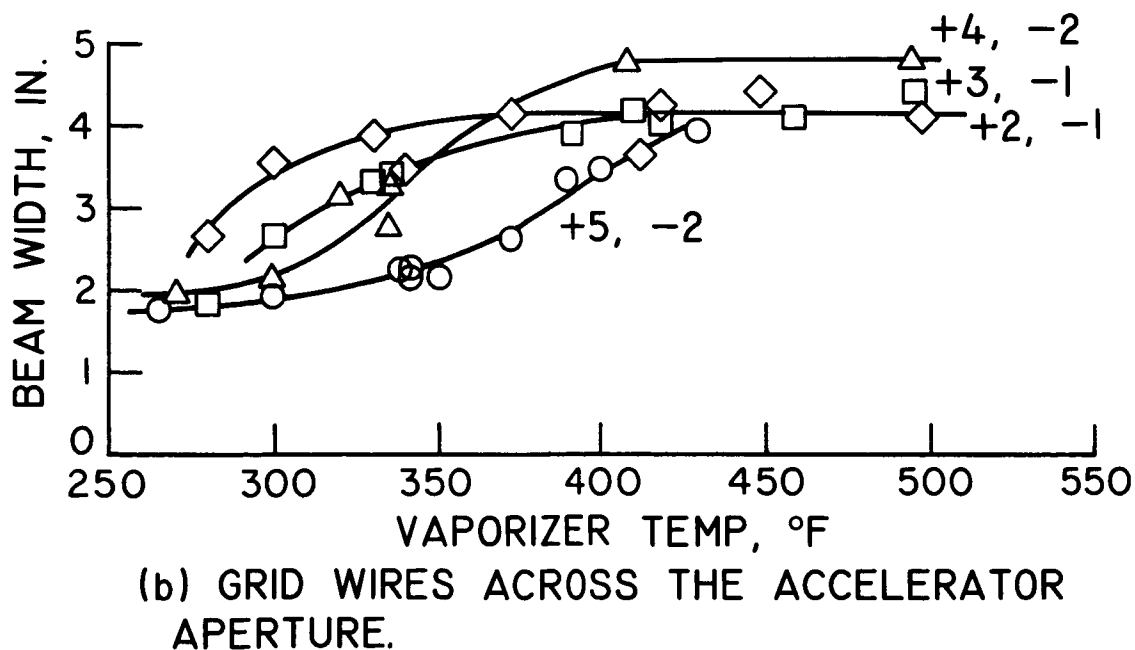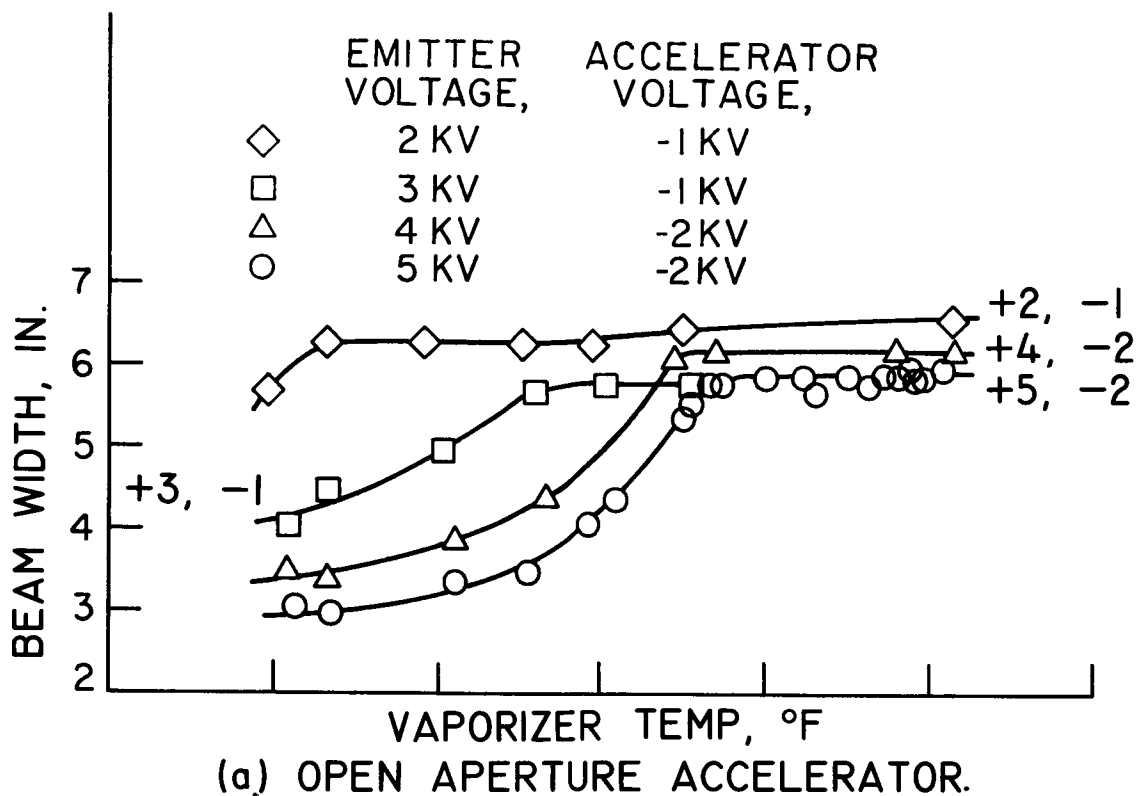
Figure 15. - Beam width as a function of vaporizer temperature at a station 7.1 inches downstream of the emitter. $Z/D = 0.87$.
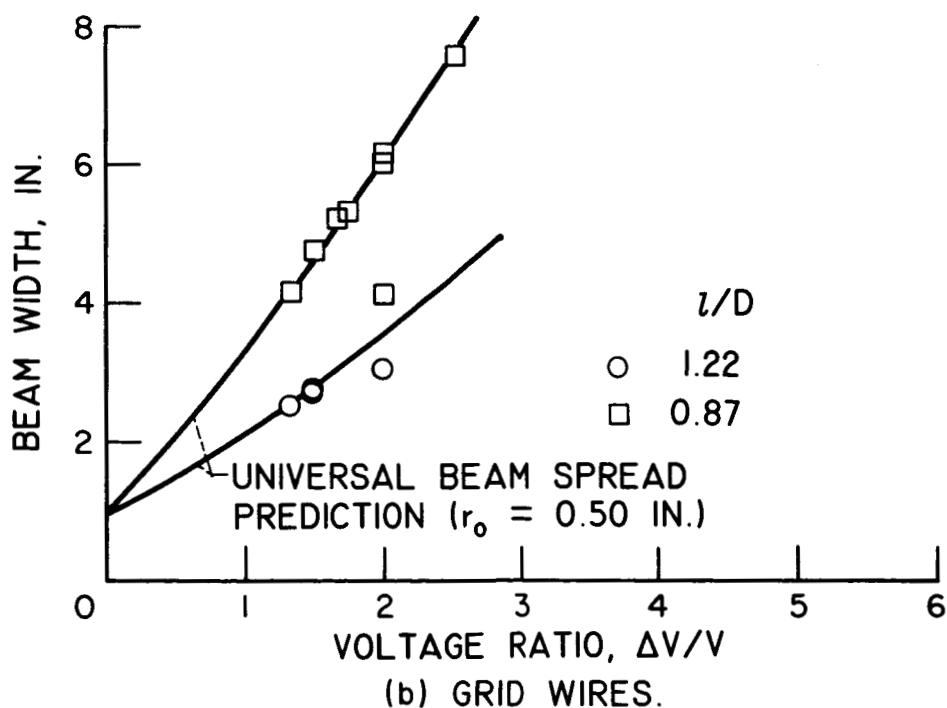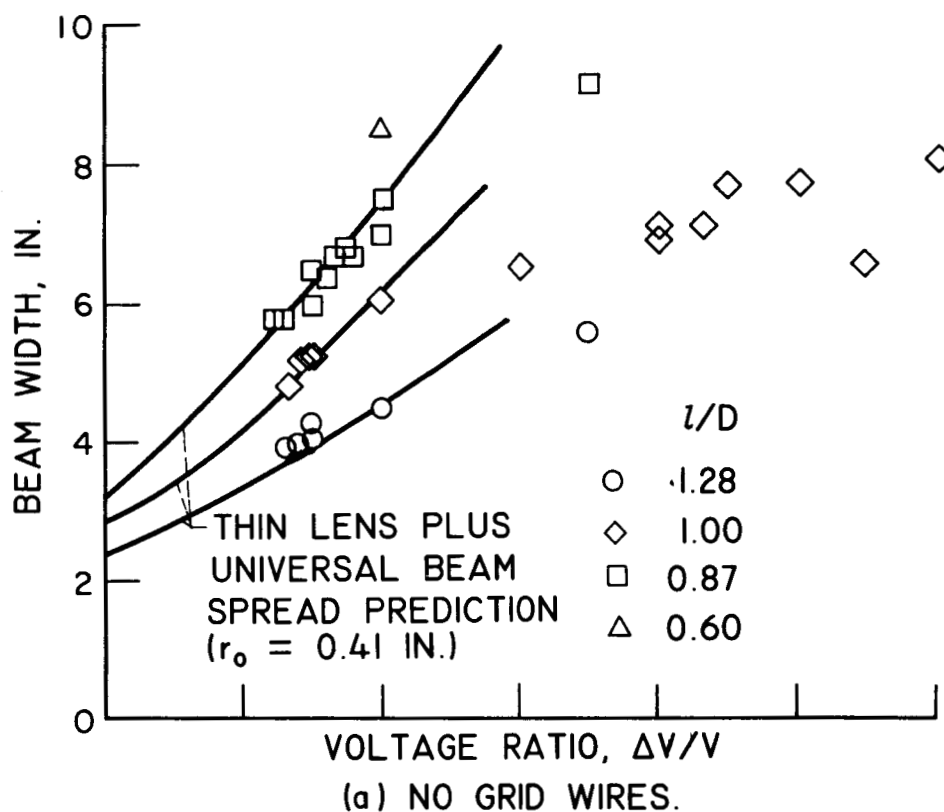
Figure 16. - Comparison of the measured space charge limited beam spreading with theoretical spreading curves. Survey station 7.1 in. downstream of ion emitter.
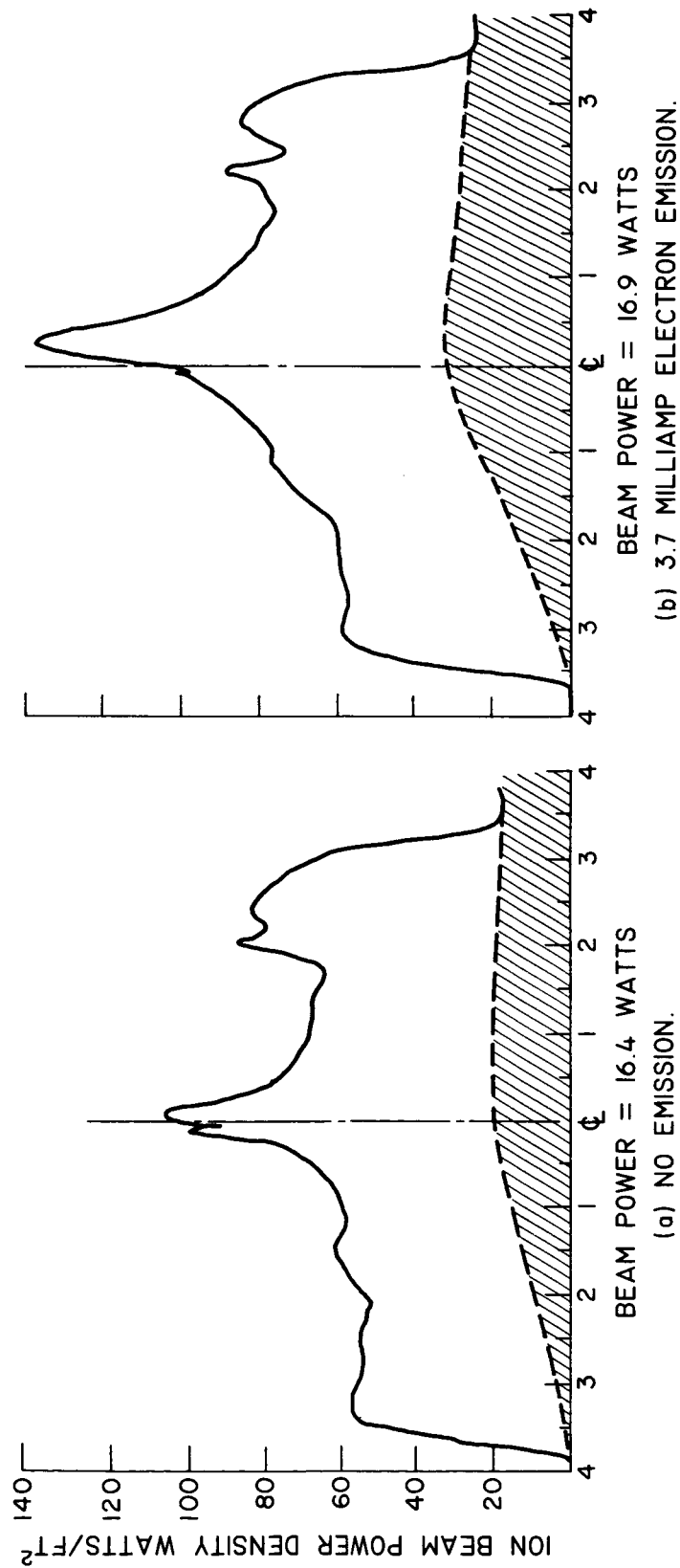
Figure 17. - Effect of neutralizer emission on beam power distribution. Emitter voltage +5 KV, accelerator voltage -5 KV.
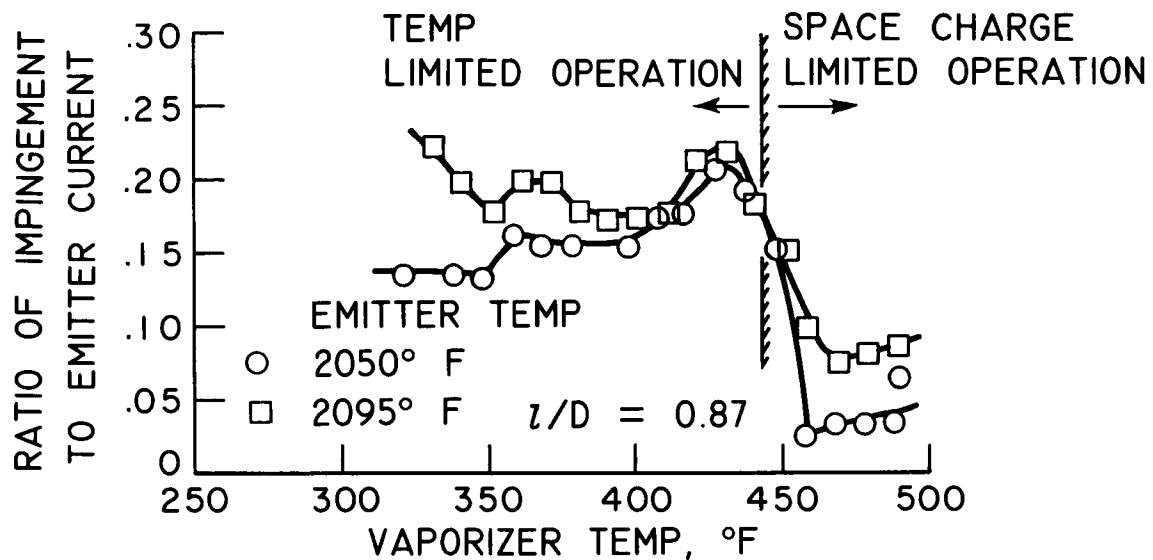
(a) EFFECT OF VAPORIZER TEMPERATURE
ON ACCELERATOR IMPINGEMENT.
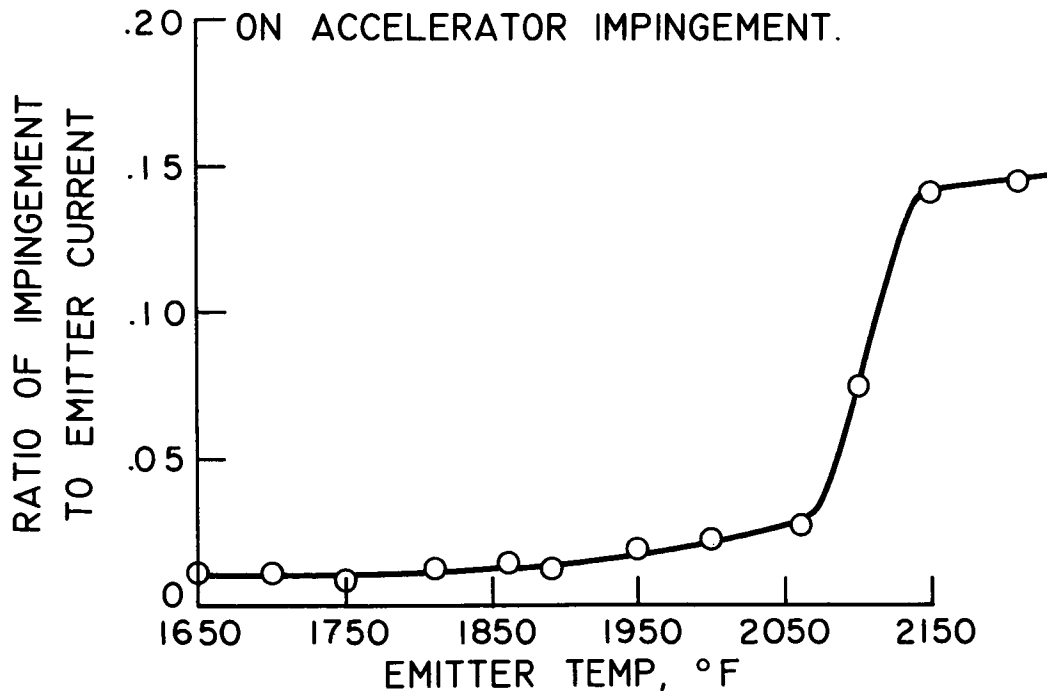
(b) EFFECT OF EMITTER TEMPERATURE
ON ACCELERATOR IMPINGEMENT.
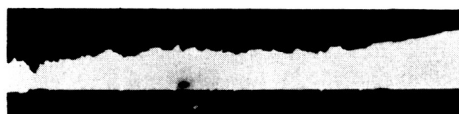$l/D = 1.28.$

Figure 18. - Accelerator impingement characteristics.
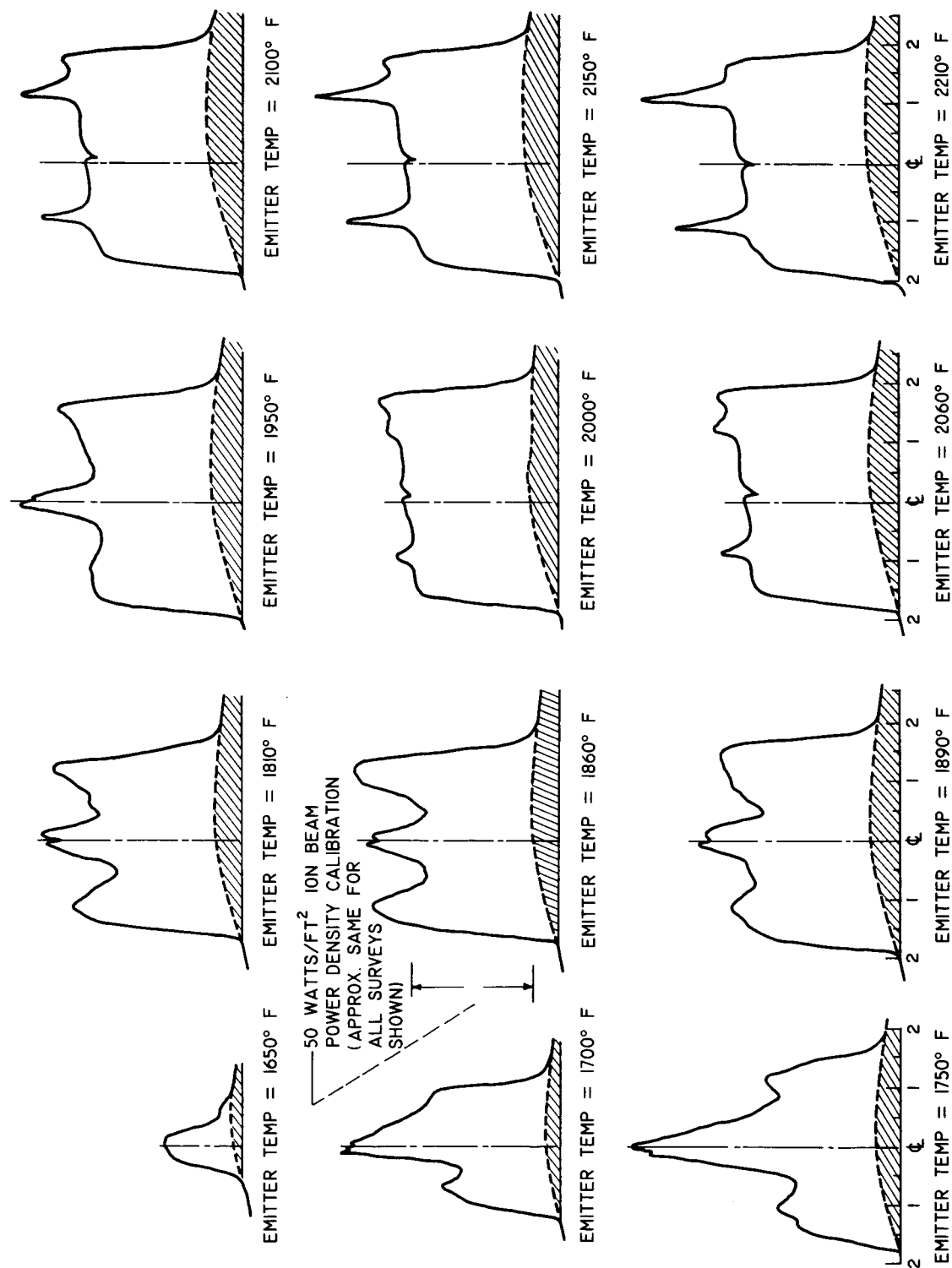
Figure 19. - Effect of accelerator impingement on the beam power distribution. $\ell/D = 1.28$.
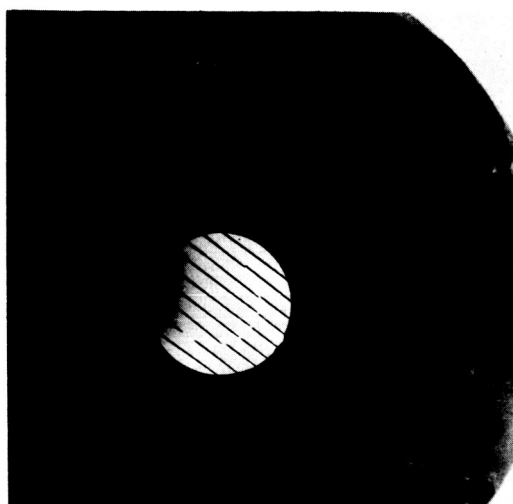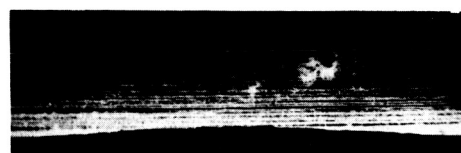
(a) NEGATIVE PIERCE ACCELERATOR WITH SPUTTERED GRID WIRES.

(b) CLOSE−UP OF SPUTTERED GRID WIRES.

(c) MICROGRAPH OF A TANTALUM GRID WIRE IN REGION OF MAXIMUM SPUTTERING.
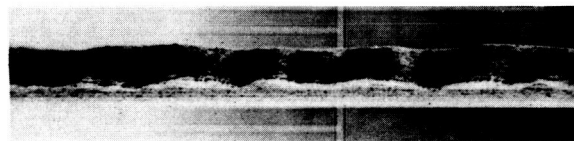
SIDE VIEW   TOP VIEW

(d) MICROGRAPHS OF A TUNGSTEN GRID WIRE IN THE REGION OF MAXIMUM SPUTTERING.

C-58826

Figure 20. - Ion sputtering of grid wires on the Pierce accelerator.
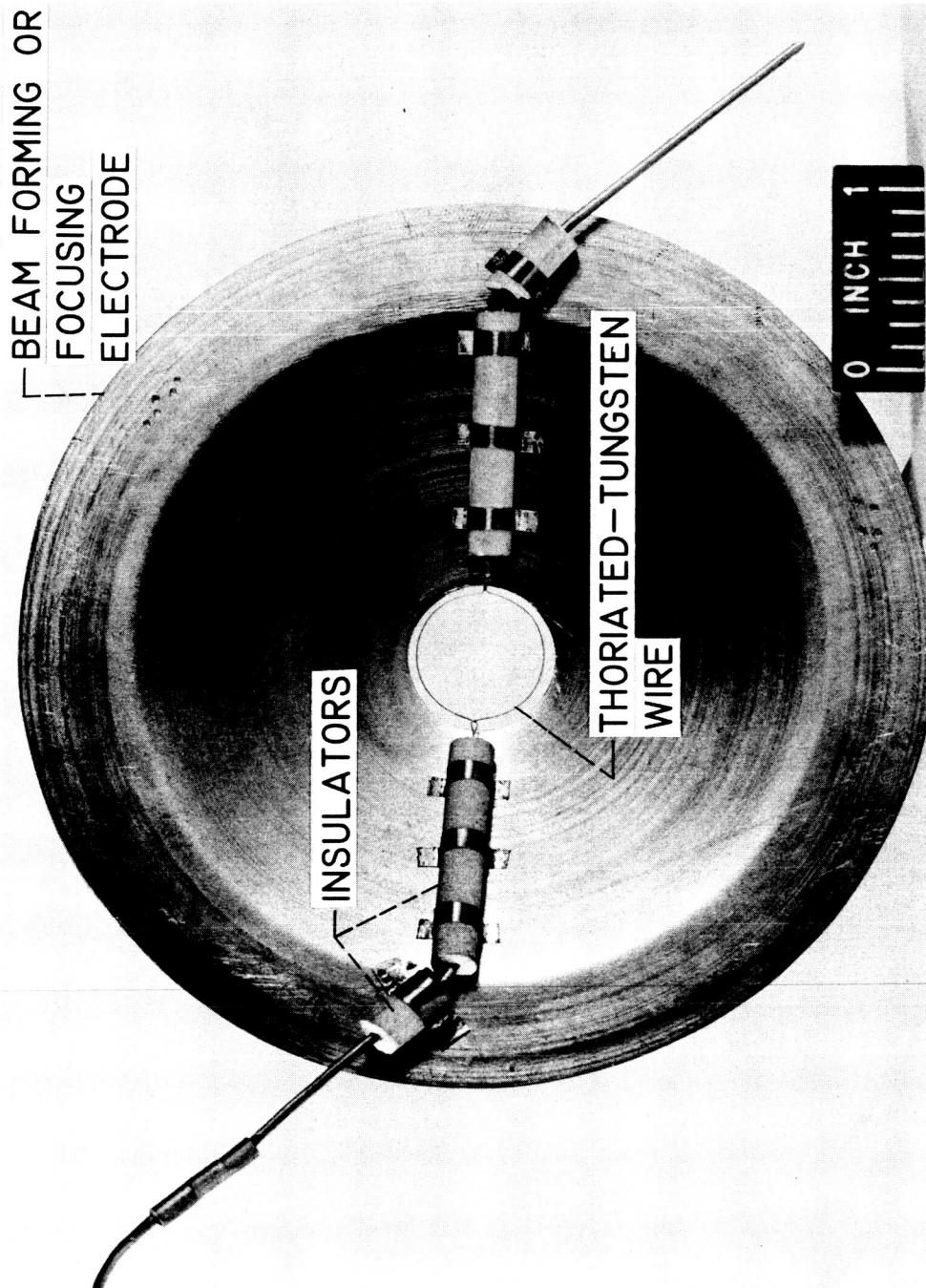
(a) NEAR BEAM EDGE.

(b) AT BEAM CENTER.

C-58827

Figure 21. - Ion sputtering of a straight
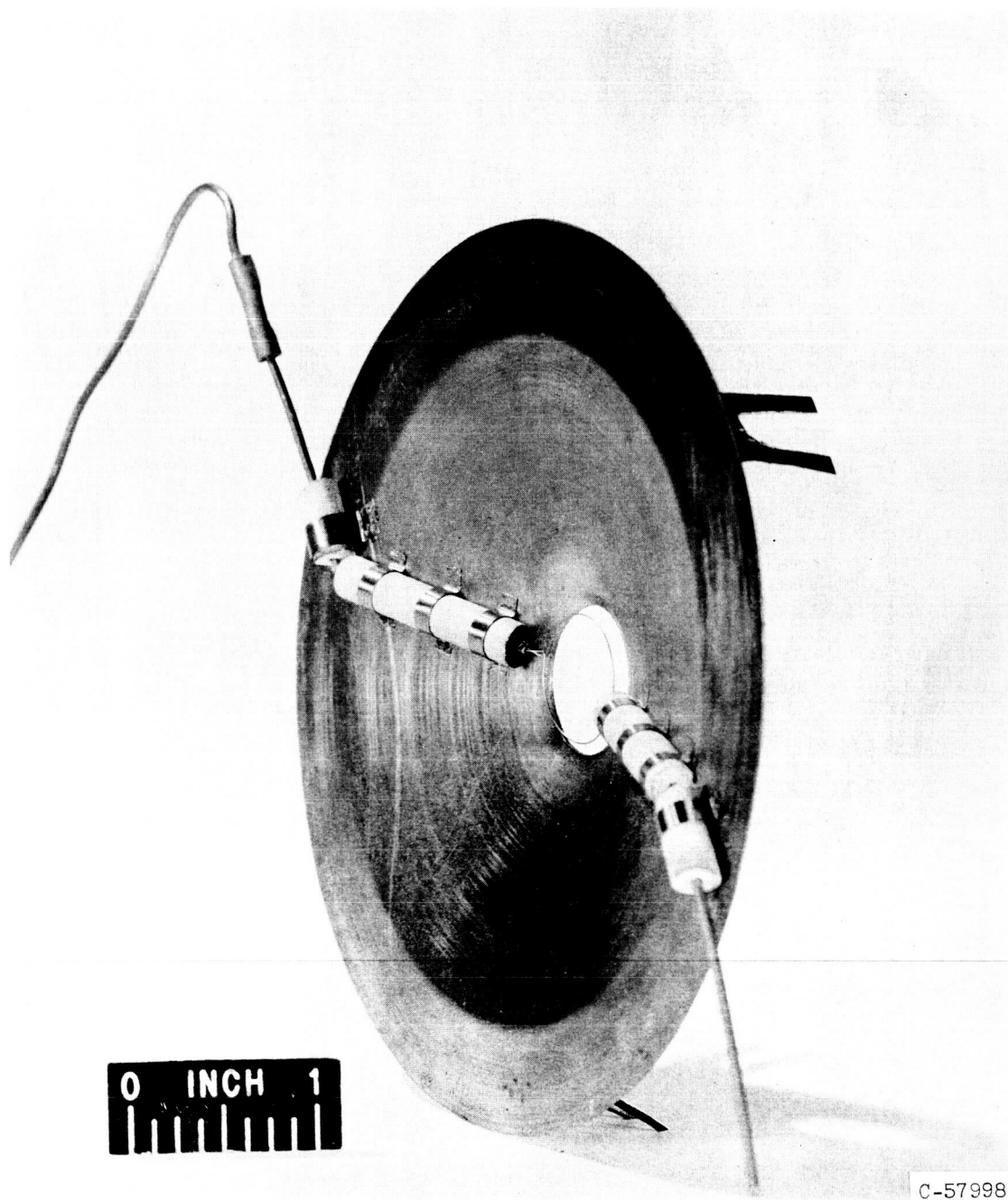tungsten grid wire accelerator.

(a) FRONT VIEW.

Figure 22. - Thoriated-tungsten wire electron emitter mounted on beam forming electrode.

(b) SIDE VIEW.

Figure 22. - Concluded. Thoriated-tungsten wire electron emitter mounted on beam forming electrode.

E-1516

VAPORIZER TEMP = 275° F

VAPORIZER TEMP = 368° F

VAPORIZER TEMP = 268° F

VAPORIZER TEMP = 375° F

NORMAL OPERATION

VAPORIZER TEMP = 405° F

VAPORIZER TEMP = 455° F

(a) NO ELECTRON EMISSION.

50 WATTS/FT² ION BEAM POWER DENSITY CALIBRATION FOR ELECTRON EMISSION DATA

DISTANCE FROM CENTERLINE, IN. VAPORIZER TEMP = 400° F

(b) DATA OBTAINED WITH ELECTRON EMITTER BETWEEN ION EMITTER AND ACCELERATOR.
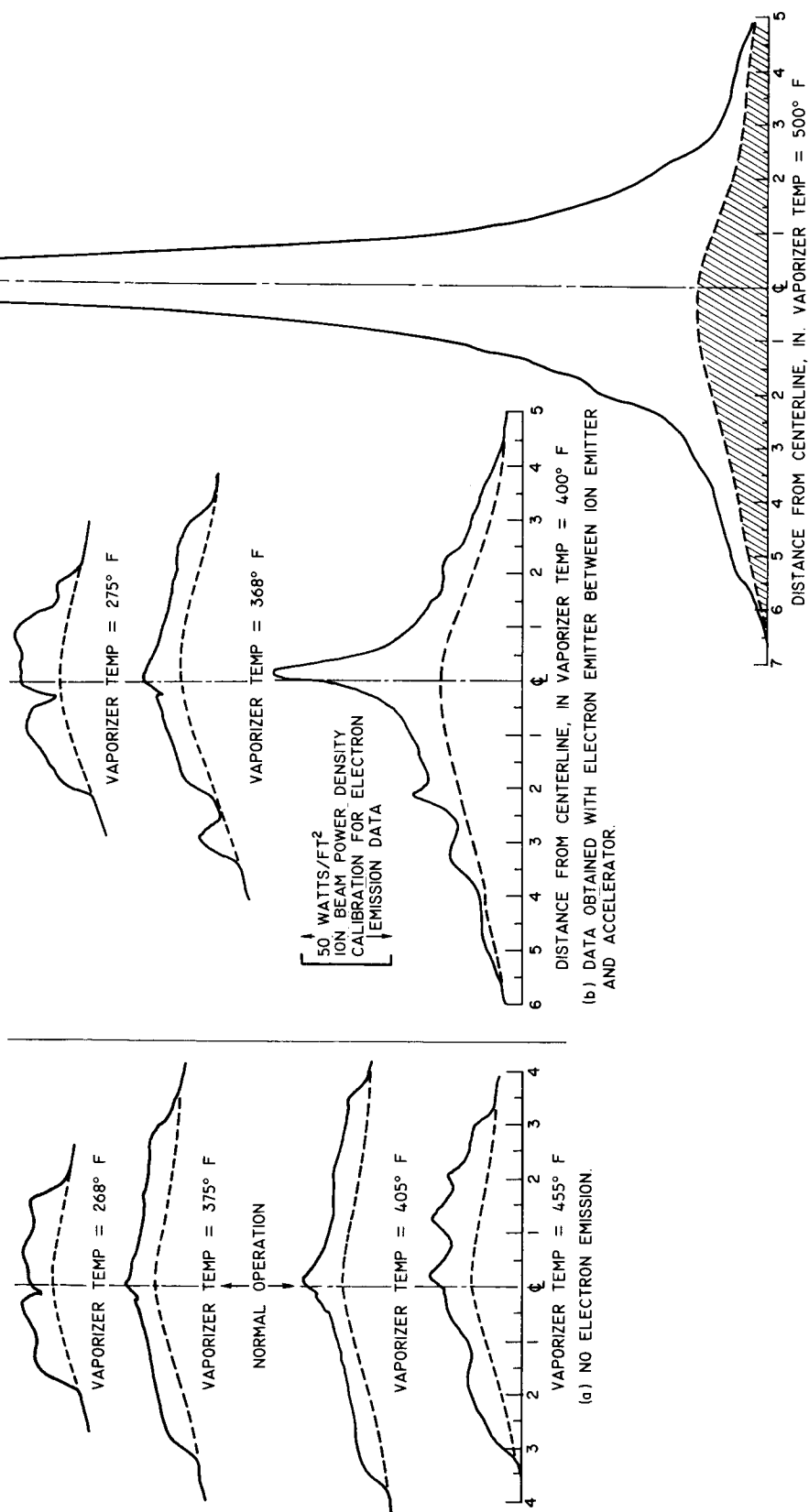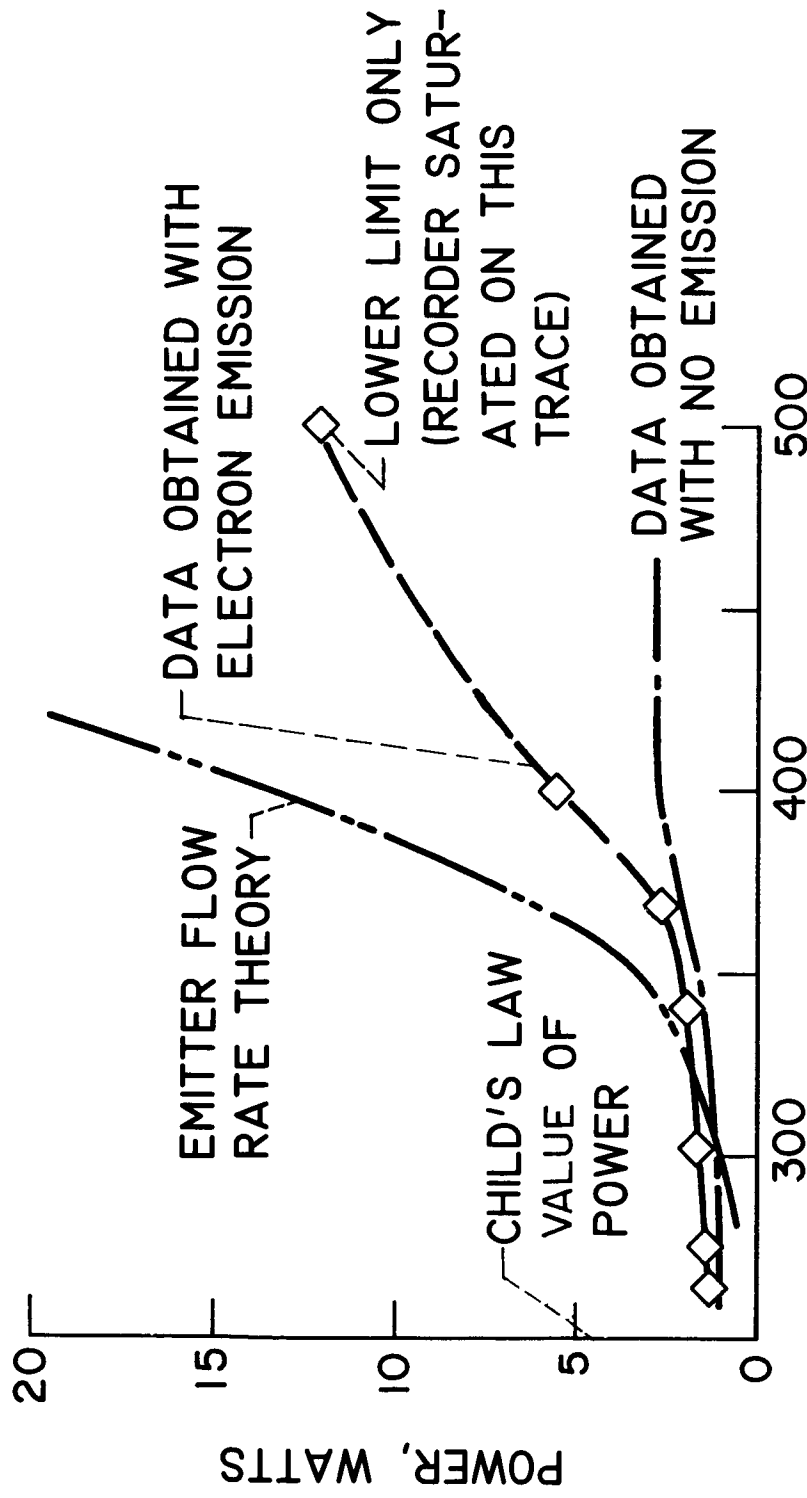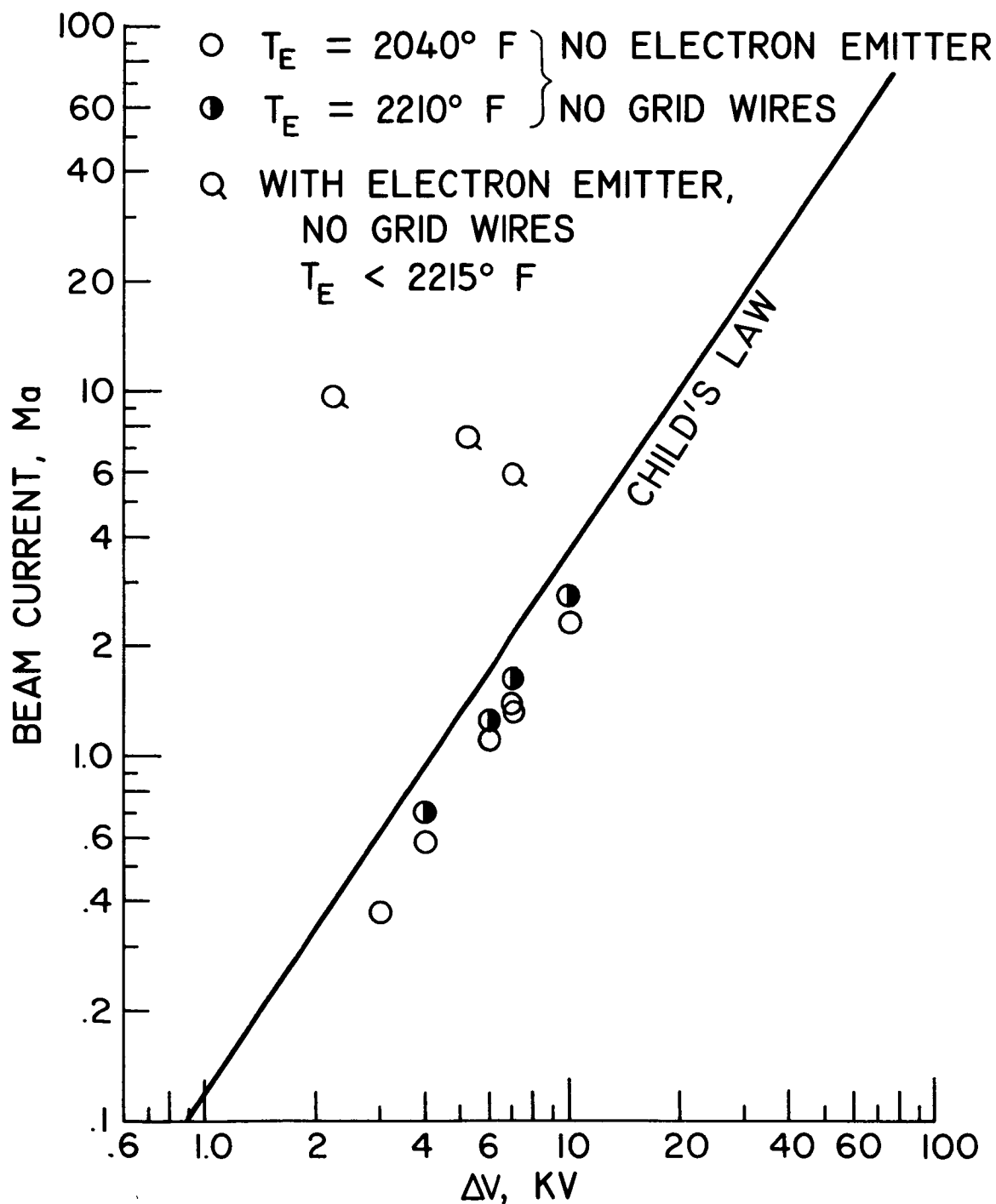
DISTANCE FROM CENTERLINE, IN. VAPORIZER TEMP = 500° F

Figure 23. – Increase in beam power available due to the electron emitter – accelerator system, $l/D = 1.0$.

(a) VAPORIZER TEMPERATURE EFFECT, EMITTER VOLTAGE + 2 KV, ACCELERATOR VOLTAGE −5 KV.

Figure 24. - Comparison of the output of the electron emitter - accelerator system with normal operation. $l/D = 1.0$.

(b) ACCELERATING VOLTAGE EFFECT.

Figure 24. - Concluded. Comparison of the output of the electron emitter - accelerator system with normal operation. $l/D = 1.0$.